

Spectroscopic properties of Er^{3+} - and Yb^{3+} -doped soda-lime silicate and aluminosilicate glasses

Markus P. Hehlen,* Nigel J. Cockcroft,[†] and T. R. Gosnell
Los Alamos National Laboratory, Mailstop E535, Los Alamos, New Mexico 87545

Allan J. Bruce
Lucent Technologies, 700 Mountain Avenue, Murray Hill, New Jersey 07974
 (Received 28 August 1996; revised manuscript received 4 April 1997)

A spectroscopic investigation of an extensive series of Er^{3+} -doped and Er^{3+} , Yb^{3+} -codoped soda-lime-silicate (SL) and aluminosilicate (AS) glasses is presented. Compared to SL glasses, 4*f* transitions in AS glasses show higher oscillator strengths, larger inhomogeneous broadening, and smaller crystal-field splittings of the respective excited-state multiplets. The Er^{3+} excited-state relaxation dynamics is adequately described by a combination of the Judd-Ofelt model and the energy-gap law. With the exception of $^4I_{13/2}$, multiphonon relaxation is dominant for all excited states, making it possible to efficiently pump the 1.55 μm $^4I_{13/2} \rightarrow ^4I_{15/2}$ emission by excitation of $^4I_{11/2}$ at around 980 nm. The absolute $^4I_{13/2}$ luminescence quantum yield, for low 980-nm excitation density ($\sim 5 \text{ W/cm}^2$), η , is ~ 0.9 at 0.4 mol % Er_2O_3 and drops to about 0.65 upon increasing Er_2O_3 to 1.2 mol %, indicating the onset of energy-transfer processes. Samples with high OH^- impurity concentration suffer from significantly higher quenching of $^4I_{13/2}$ luminescence at higher Er^{3+} concentrations. Energy migration to the minority of Er^{3+} ions coordinated to OH^- , followed by efficient multiphonon relaxation accounts for this effect. At low excitation densities, the strong near-infrared absorption of Yb^{3+} in combination with efficient $\text{Yb} \rightarrow \text{Er}$ energy transfer increases the $^4I_{13/2}$ population density in Yb^{3+} , Er^{3+} -codoped samples by up to 2 orders of magnitude compared to equivalent samples without Yb^{3+} . The dependence of η on Yb^{3+} codotation of 0.4 mol % Er_2O_3 -doped samples predicts that a minimum of ~ 0.8 mol % Yb_2O_3 is required to achieve efficient sensitization of Er^{3+} by Yb^{3+} . The relative intensities of upconversion luminescence from $^4S_{3/2}$ and $^2H_{11/2}$ are used to analyze internal sample heating in detail. Due to the high absorption cross section of Yb^{3+} , increasing the Yb^{3+} concentration in Yb^{3+} , Er^{3+} -codoped samples of given length increases the absorbed power and subsequently the total density of multiphonon emission, leading to internal temperatures of up to 572 K in 0.4 mol % Er_2O_3 samples codoped with 4 mol % Yb_2O_3 and excited with 51 kW/cm^2 . Multiphonon relaxation from $^4I_{13/2}$ is shown to be inefficient even at these high internal sample temperatures. From upconversion luminescence spectra of a series of glasses, the thermal conductivity is estimated to be between 3.5×10^{-2} and $7.7 \times 10^{-2} \text{ W m}^{-1} \text{ K}^{-1}$, in good agreement with the known value of $4.8 \times 10^{-2} \text{ W m}^{-1} \text{ K}^{-1}$ for soda-lime-silicate glass. [S0163-1829(97)03436-X]

I. INTRODUCTION

In the last decade, the erbium ion (Er^{3+}) has established a key role as the active ion in optical signal amplification for the 1.55 μm telecommunications wavelength.¹ In long-distance optical networks, signal amplification is required to compensate for losses in the silica fiber, and with the use of Er^{3+} systems, all-optical amplification rather than electro-optical regeneration can be achieved.² The superb performance of silica optical fibers and of Er^{3+} -doped fiber amplifiers EDFA's has led to a revolution in high-speed optical telecommunications, enabling deployment of high-capacity fiber-optic links on a global scale.

The energy-level structure of Er^{3+} , depicted in Fig. 1, permits pumping of the $^4I_{11/2}$ excited-state multiplet around 980 nm by semiconductor lasers, and the $^4I_{13/2}$ excited-state multiplet is populated by subsequent multiphonon relaxation. Radiative relaxation of $^4I_{13/2}$ to the $^4I_{15/2}$ ground-state multiplet may then provide gain around 1.55 μm , a wavelength which matches the attenuation minimum of silica optical fibers. The significant inhomogeneous broadening of the Er^{3+} optical transitions in the disordered glass hosts allows for wavelength multiplexing, and it is possible to simultaneously

operate several wavelength channels at multigigabit per s data transmission rates in a single fiber-optical link.²

Planar-optical-waveguide amplifiers (POWA's), for example waveguides fabricated on silicon wafers by silicon optical-bench processing techniques, are a variation of optical fiber amplifiers. A POWA component can integrate waveguides, semiconductor diode lasers, and a variety of passive optical elements on a single silicon chip, and it may thus provide the significant reduction in both device size and cost desired for all-optical local-area networks. This potential for miniaturization of optical amplifiers has inspired considerable research interest in new Er^{3+} -based amplifier materials.³⁻⁹ The restriction to compact (cm-scale) device lengths in POWA's requires, in order to achieve sufficient pump-light absorption and net gain, much higher Er^{3+} concentrations than the typical 100–300 ppm doping used in the several-tens-of-meters long EDFA's. Recently, the feasibility of POWA's has been demonstrated,¹⁰⁻¹² and the highest net gain of 15 dB was observed in a 14 600 ppm Er^{3+} -doped 4.5-cm-long soda-lime-silicate planar waveguide pumped at 980 nm with 280 mW.¹² This Er^{3+} concentration is 100 times higher than the concentrations typically used in EDFA's and the reduction in active length is substantial. At

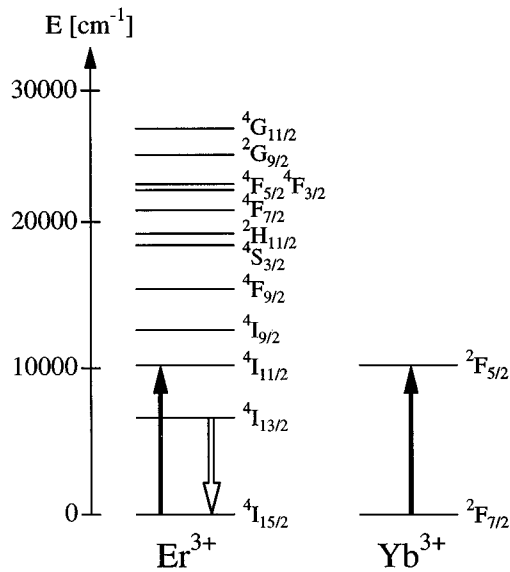


FIG. 1. Energies of 2^S+1L_J multiplets of Er^{3+} and Yb^{3+} . Only Er^{3+} multiplets in the energy range relevant to this study are shown. The solid arrows indicate the transitions used for excitation of the $1.55\ \mu\text{m}$ ($4I_{13/2} \rightarrow 4I_{15/2}$) Er^{3+} luminescence transition (open arrow).

these high Er^{3+} concentrations, however, energy-transfer processes between two or more Er^{3+} ions, such as upconversion or energy migration to parasitic impurities, can become important and degrade the luminescence quantum yield from the most important excited-state multiplet, $4I_{13/2}$. Together with the intrinsically low absorption cross section of Er^{3+} for 980-nm pump light, this adversely affects both the threshold power and the gain per unit length and limits further optimization of Er^{3+} -based POWA's. The use of ytterbium (Yb^{3+}) as a sensitizer for Er^{3+} , a mechanism that has been known for a long time,¹³ offers attractive alternatives to POWA materials doped only with Er^{3+} . The $2F_{7/2} \rightarrow 2F_{5/2}$ transition of Yb^{3+} in the near infrared (see Fig. 1) has a high absorption cross section and, in combination with efficient $\text{Yb} \rightarrow \text{Er}$ energy transfer, may allow for a considerable reduction of Er^{3+} concentrations while maintaining sufficient pump-light absorption, making it possible to design short POWA devices requiring only low excitation intensities.

The realization of Yb^{3+} -sensitized Er^{3+} -based POWA's involves optimization of a variety of parameters and therefore requires a detailed knowledge of the excited-state dynamics in order to design glasses with loss rates within acceptable limits. This paper presents a detailed spectroscopic investigation of an extensive series of Er^{3+} -doped and Yb^{3+} , Er^{3+} -codoped soda-lime-silicate and aluminosilicate bulk glasses. Compared to pure silica glass, soda-lime-silicate and aluminosilicate glasses offer a 10–20 times greater solubility for rare-earth ions without forming ion clusters. In addition, the various constituents of soda-lime-silicate and aluminosilicate glasses provide a much wider range for chemical modifications than pure silica. The dependence of the Er^{3+} oscillator strengths on the glass composition is discussed on the basis of a Judd-Ofelt intensity analysis. Of particular interest is the origin of the spectral structure in the $1.55\text{-}\mu\text{m}$ emission band and methods to smooth this spectral gain profile. Absolute luminescence quantum-

yield measurements are used to establish useful Er^{3+} and Yb^{3+} concentration regimes and to identify the efficient quenching of $4I_{13/2}$ population at OH^- impurity sites. A detailed analysis of internal sample heating and its relevance to the $4I_{13/2}$ radiative relaxation properties is presented.

II. EXPERIMENT

A. Sample preparation

Soda-lime-silicate glasses were prepared from >99.999% cationic purity powders of SiO_2 , Na_2O , CaO , MgO , B_2O_3 , Li_2O , GeO_2 , Sc_2O_3 , La_2O_3 , Er_2O_3 , and Yb_2O_3 , melted in Pt crucibles at $1400\ ^\circ\text{C}$ for up to 50 h under dry air (<1 ppm H_2O) in a resistance furnace, and cooled *in situ*. Soda-lime-silicate glass series with a total rare-earth oxide concentration of 0.4, 1.25, 2.5, and 5 mol % with fixed 0.4 mol % Er_2O_3 were prepared. For aluminosilicate glasses, the >99.999% cationic purity SiO_2 , Al_2O_3 , CaO , MgO , BaO , P_2O_5 , B_2O_3 , La_2O_3 , Er_2O_3 , and Yb_2O_3 were used in a similar preparation. Aluminosilicate glass series with a total rare-earth-oxide concentration of 2.5, 5, 10, and 15 mol % with fixed 0.4 mol % Er_2O_3 and Al_2O_3 concentrations ranging from 9 to 25 mol % were prepared. For both glass types, concentration series of Er_2O_3 (0.05–1.2 mol %) and concentration series of 0.4 mol % Er_2O_3 samples codoped with Yb_2O_3 (0.2–4.0 mol %) were prepared. All samples were cut to rectangular parallelepipeds and optically polished. The physical characterization of the samples included measurements of the density, refractive index, and Er^{3+} and Yb^{3+} ion densities. The compositions of all glasses used in this study are listed in Table I.

B. Spectroscopic experiments

With one exception, all experiments were carried out at room temperature. Absorption spectra in the visible, near-infrared, and midinfrared spectral range were recorded on a Cary 5E (Varian) and a FTS40 (Bio-Rad) dry N_2 purged spectrometer, respectively.

An argon-ion laser pumped Ti:sapphire laser was used to excite the samples around 980 nm for the continuous-wave luminescence spectra in the visible (VIS) and near-infrared (NIR) spectral regions, and for the lifetime measurements of the $1.55\text{-}\mu\text{m}$ emission of Er^{3+} . Sample luminescence was dispersed by a 1-m monochromator (spectral resolution $1.5\ \text{cm}^{-1}$ and $5\ \text{cm}^{-1}$ in the NIR and VIS, respectively) and was detected using a cooled InGaAs diode (NIR) or a photomultiplier (VIS) in combination with a lock-in amplifier.

A Nd:YAG pumped pulsed dye laser operating around 698 nm (LDS 698) was Raman shifted in H_2 to produce pulsed (8 ns, 10 Hz) excitation in the 980-nm range for the measurements of upconversion luminescence spectra at low excitation densities. The same mode of excitation was used for the measurement of temperature-dependent lifetimes of the $1.55\text{-}\mu\text{m}$ emission of Er^{3+} . For this experiment, samples were either cooled by a closed-cycle refrigerator or heated in a controlled heated resistance furnace.

Absolute luminescence quantum yields for the $4I_{13/2} \rightarrow 4I_{15/2}$ transition around $1.55\ \mu\text{m}$ for excitation around 980 nm were obtained from luminescence spectra recorded with the sample placed in a 6-in. Spectralon®-

TABLE I. Glass composition, glass density ρ (g cm^{-3}), and refractive index n at 589 nm for the soda-lime-silicate (top section) and aluminosilicate (bottom section) bulk glasses used in this study. The Judd-Ofelt intensity parameters $\Omega_{(\lambda)}$ (10^{-20} cm^2), obtained from an intensity-weighted least-squares fit of the oscillator strengths (see Fig. 2) to Eqs. (1) and (2) [using the atomic parameters $F_{(2)}=422.45 \text{ cm}^{-1}$, $F_{(4)}=65.05 \text{ cm}^{-1}$, $F_{(6)}=6.743 \text{ cm}^{-1}$, $\zeta=2371 \text{ cm}^{-1}$ (Ref. 17)], the full spectral width at half maximum FWHM (cm^{-1}) (obtained from a Gaussian fit to the highest-energy ${}^4I_{15/2} \rightarrow {}^4I_{13/2}$ absorption peak, see inset Fig. 2), and the ratio of nonbridging oxygen (NBO) versus total rare-earth (RE^{3+}) concentrations, γ [calculated from the glass composition (see Sec. IV B)] are shown for selected, representative samples.

Glass composition (mol % of the respective oxide)														Judd-Ofelt parameters (10^{-20} cm^2)			FWHM	γ		
Si	Na	Al	Ca	Mg	Ba	Li	P	Ge	B	Sc	La	Er	Yb	ρ (g cm^{-3})	n	$\Omega_{(2)}$	$\Omega_{(4)}$		$\Omega_{(6)}$	(cm^{-1})
72.42	13.57		8.81	3.95							1.20	0.05		2.58	1.526					
72.42	13.57		8.81	3.95							1.15	0.10		2.58	1.526					
72.42	13.57		8.81	3.95							1.05	0.20		2.58	1.526					
72.42	13.57		8.81	3.95							0.85	0.40		2.58	1.525	4.32	0.83	0.41	201	24.1
72.42	13.57		8.81	3.95							0.45	0.80		2.59	1.524					
72.42	13.57		8.81	3.95							0.05	1.20		2.61	1.523					
72.42	13.57		8.81	3.95							0.05	0.80	0.40	2.61	1.521					
72.42	13.57		8.81	3.95							0.45	0.40	0.40	2.60	1.522					
72.42	13.57		8.81	3.95							0.65	0.20	0.40	2.60	1.523					
71.70	14.70		4.00	8.80								0.83		2.53	1.511					
72.20	14.80		4.00	8.90								0.14		2.43	1.504					
72.00	14.70		4.00	8.90								0.41		2.47	1.508					
73.02	13.69		8.88	3.98								0.20	0.20	2.51	1.514					
73.02	13.69		8.88	3.98								0.40		2.51	1.516					
73.02	13.69		8.88	3.98							0.20	0.20		2.49	1.514					
72.40	13.57		8.81	3.95							0.05	0.80	0.40	2.60	1.522					
72.40	13.57		8.81	3.95							0.45	0.40	0.40	2.59	1.523					
72.40	13.57		8.81	3.95							0.05	0.40	0.80	2.61	1.522					
72.40	13.57		8.81	3.95							0.85	0.20	0.20	2.58	1.523					
72.40	13.57		8.81	3.95							0.65	0.20	0.40	2.58	1.524					
72.40	13.57		8.81	3.95							0.25	0.20	0.80	2.60	1.521					
70.98	13.30		8.64	3.87					1.96		0.83	0.39		2.58	1.528					
70.98	13.30		8.64	3.87					1.96		0.64	0.20	0.39	2.60	1.527					
70.98	13.30		8.64	3.87					1.96		1.03	0.20		2.61	1.526					
73.00	13.70		8.90	4.00								0.40		2.53	1.519	4.56	0.83	0.35	196	69.5
69.60	13.10		8.50	3.80							4.60	0.40		2.97	1.571	5.31	1.11	0.51	218	8.08
69.60	13.10		8.50	3.80							2.60	0.40	2.00	3.01	1.565					
69.60	13.10		8.50	3.80					2.00		2.60	0.40		2.84	1.573					
69.60	13.10		8.50	3.80					2.00		0.60	0.40	2.00	2.91	1.560					
69.60	13.10		8.50	3.80							0.60	0.40	4.00	3.09	1.568					
71.50	13.40		8.70	3.90							2.10	0.40		2.71	1.539	4.94	0.89	0.46	208	13.4
71.50	13.40		8.70	3.90							0.10	0.40	2.00	2.78	1.534					
71.50	13.40		8.70	3.90							0.50	0.40	1.60	2.78	1.538					
71.50	13.40		8.70	3.90							0.90	0.40	1.20	2.76	1.537					
71.50	13.40		8.70	3.90							1.30	0.40	0.80	2.75	1.538					
71.50	13.40		8.70	3.90							1.50	0.40	0.60	2.73	1.530					
71.50	13.40		8.70	3.90							1.70	0.40	0.40	2.72	1.537					
71.50	13.40		8.70	3.90							1.90	0.40	0.20	2.71	1.538					
69.70	13.20		8.50	3.80					2.30		0.10	0.40	2.00	2.79	1.537					
61.50	13.40		8.70	3.90				10.00			0.10	0.40	2.00	2.96	1.552					
69.60	6.55		8.50	3.80		6.55					4.60	0.40		2.95	1.581	5.05	1.09	0.61		8.08
65.00		20.00									14.95	0.05		3.57	1.652					
65.00		20.00									14.90	0.10		3.57	1.652					
65.00		20.00									14.80	0.20		3.57	1.652					
65.00		20.00									14.60	0.40		3.57	1.652					
65.00		20.00									14.20	0.80		3.58	1.652					

TABLE I. (Continued.)

Glass composition (mol % of the respective oxide)														Judd-Ofelt parameters (10 ⁻²⁰ cm ²)			FWHM (cm ⁻¹)	γ			
Si	Na	Al	Ca	Mg	Ba	Li	P	Ge	B	Sc	La	Er	Yb	ρ (g cm ⁻³)	n	$\Omega_{(2)}$	$\Omega_{(4)}$	$\Omega_{(6)}$			
65.00		20.00									13.80	1.20		3.59	1.652						
70.00		15.00									14.60	0.40		3.55	1.646	6.41	1.42	0.82	259	2.00	
65.00		20.00									14.20	0.40	0.40	3.59	1.651						
65.00		20.00									13.80	0.40	0.80	3.60	1.651						
65.00		20.00									14.40	0.20	0.40	3.58	1.651						
65.00		20.00									14.00	0.20	0.80	3.59	1.651						
60.60		9.40	11.40	11.20	2.50						2.60	0.40	2.00	3.23	1.602						
60.60		9.40	11.40	11.20	2.50						0.60	0.40	4.00	3.23	1.592						
60.60		9.40	11.40	11.20	2.50					2.00	2.60	0.40		3.02	1.600	5.46	1.61	0.85			6.14
60.60		9.40	11.40	11.20	2.50					2.00	0.60	0.40	2.00	3.09	1.594						
60.60		9.40	11.40	11.20	2.50						4.60	0.40		3.12	1.606	5.44	1.55	0.84			6.14
57.50		8.90	10.80	10.60	2.40				4.80		0.60	0.40	4.00	3.25	1.591						
58.20		9.00	10.90	10.80	2.40		1.90				0.60	0.40	3.80	3.17	1.585						
62.10		9.60	11.70	11.50	2.60						2.10	0.40		2.90	1.572	5.68	1.45	0.80			9.48
62.10		9.60	11.70	11.50	2.60						0.10	0.40	2.00	2.88	1.567						
62.10		9.60	11.70	11.50	2.60						0.50	0.40	1.60	2.85	1.569						
62.10		9.60	11.70	11.50	2.60						0.90	0.40	1.20	2.93	1.570						
62.10		9.60	11.70	11.50	2.60						1.30	0.40	0.80	2.93	1.571						
63.20		8.90	25.40								2.10	0.40		2.87	1.582	6.24	1.30	0.74	252	9.60	
63.20		8.90	25.40								0.10	0.40	2.00	2.92	1.578						
65.00		25.00									9.60	0.40		3.25	1.614	7.14	1.58	0.92	270	0.50	
65.00		25.00									7.60	0.40	2.00	3.29	1.610						
65.00		25.00									5.60	0.40	4.00	3.38	1.608						

coated integrating sphere and excited by an argon-ion laser-pumped Ti:sapphire laser. The luminescence was dispersed by a 0.25-m monochromator and detected as described above. The absolute spectral response of the setup was determined from a measurement of a NIST-calibrated coiled-coil tungsten lamp operated by a high-precision constant-current source. The total emission rate around 1.55 μm was calculated by numerical integration of the corrected spectral profile and subsequent application of a reabsorption correction factor obtained from a geometrical Monte Carlo simulation of radiation trapping.¹⁴ The absorption coefficient at the excitation wavelength and the refractive index were used to calculate the total absorption rate considering multiple internal reflection in the sample. The absolute accuracy of the results was verified by cross-checking luminescence quantum yields for well-known commercial Nd³⁺-doped laser glasses (LG750 and LG760, from Schott Glass Technologies, Duryea, PA).¹⁵

III. RESULTS

Figure 2 presents representative near-infrared and visible absorption spectra of Er³⁺-doped soda-lime-silicate (SL) and aluminosilicate (AS) glasses as well as of Yb³⁺-doped aluminosilicate (AS) glass at room temperature. The energies and relative extinction coefficients for transitions to the various ^{2S+1}L_J excited-state multiplets are typical for both ions in an oxide glass environment. In contrast to the many excited-state multiplets of Er³⁺, the Yb³⁺ ion has only one

excited-state multiplet (²F_{5/2}), and the respective absorptions from the ²F_{7/2} ground-state multiplet are observed around 10 245 cm⁻¹ (976 nm). The peak absorption cross section as well as the oscillator strength of ²F_{7/2}→²F_{5/2} are more than an order of magnitude greater than for the Er³⁺ ⁴I_{15/2}→⁴I_{11/2} absorptions in this energy range. The disordered glass structure leads to significant inhomogeneous broadening of all the lines. Both the linewidths and the oscillator strengths are greater for AS glass than for SL glass for all the transitions in this energy range. The inset, which shows the glass samples with the largest (AS) and smallest (SL) broadening, illustrates that the overall five-peak structure as well as the total energy width of the ⁴I_{15/2}→⁴I_{13/2} (1.52 μm) absorption band is similar in both AS and SL glass. Although much sharper, the various ⁴I_{15/2}→⁴I_{13/2} crystal-field transitions of a Y₂O₃:1% Er³⁺ single crystal at room temperature show, qualitatively, a similar spectral structure.

A representative, room-temperature luminescence spectrum obtained for continuous-wave ⁴I_{15/2}→⁴I_{11/2} excitation (980 nm) of an Er³⁺-doped SL glass is shown in Fig. 3. Luminescence from the excited ⁴I_{11/2} state is almost absent whereas intense luminescence from ⁴I_{13/2} is observed. This is indication for a high efficiency of the nonradiative relaxation of ⁴I_{11/2} to ⁴I_{13/2}. Evidence for efficient ⁴I_{11/2} relaxation is also found in the luminescence transients of both these states. As shown in the left inset, the decay of ⁴I_{11/2} population is directly correlated to the fast rise of ⁴I_{13/2}

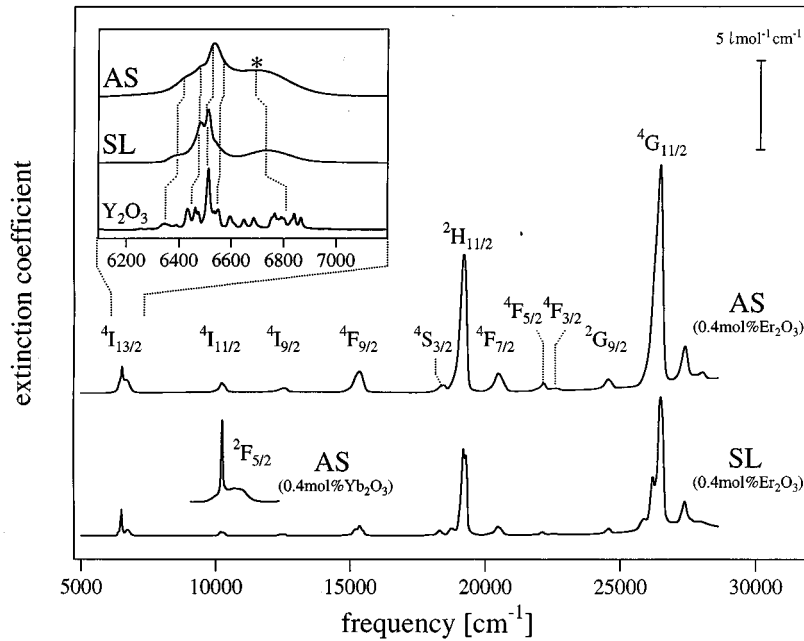


FIG. 2. Room-temperature absorption spectra representative of Er³⁺-doped soda-lime-silicate (SL) and aluminosilicate (AS) glass, and Yb³⁺-doped aluminosilicate (AS) glass. The inset shows the ⁴I_{15/2} → ⁴I_{13/2} transition for SL and AS glass and for a Y₂O₃:1% Er³⁺ crystal. The peak used to analyze changes in the inhomogeneous broadening (Secs. IV A and IV B) is marked with an asterisk.

population, both time constants obtained from single exponential fits being identical (7.5 μs) within the experimental accuracy. Besides near-infrared luminescence, weak upconversion luminescence from ²H_{11/2}, ⁴S_{3/2}, and ⁴F_{9/2} is observed in the visible range. The relative intensities of the various Er³⁺ radiative transitions in these silica-based glasses are very different from those observed in low-phonon glasses (and crystals) such as the fluorozirconate glass ZBLAN (53 ZrF₄–20 BaF₂–3.5 LaF₃–3.5 AlF₃–20 NaF). In Fig. 3, the ⁴I_{11/2} excited luminescence spectrum of ZBLAN:0.3 wt % ErF₃ is shown to scale for comparison. In ZBLAN:Er³⁺, the multiphonon relaxation of ⁴I_{11/2} is strongly suppressed, giving rise to a pronounced increase of ⁴I_{11/2} as well as upconversion luminescence at the expense of ⁴I_{13/2} luminescence. Between 13 000 and 20 000 cm⁻¹, the integrated upconversion luminescence intensity is

4.2 × 10⁵ times greater in ZBLAN:0.3 wt % ErF₃ (0.37 × 10²⁰ Er³⁺ cm⁻³) than in SL:0.4 mol % Er₂O₃ (1.97 × 10²⁰ Er³⁺ cm⁻³) for the same absorbed (⁴I_{11/2}) power. The right inset illustrates the decrease of upconversion luminescence from ²H_{11/2} relative to luminescence from ⁴S_{3/2} with the temperature decreasing from 300 to 20 K in a 0.4 mol % Er₂O₃-doped soda-lime-silicate excited around 980 nm with low (pulsed) intensity.

The dependence of the Judd-Ofelt intensity parameters Ω₍₂₎ and Ω₍₆₎ (obtained from an intensity-weighted least-squares-fitting procedure) on the ratio of nonbridging oxygen (NBO) versus total rare-earth (RE) ion concentrations, γ, is shown in Fig. 4, which includes data of several SL and AS glasses used in this study. The Ω₍₂₎ and Ω₍₆₎ parameter values are used as a linear measure for the average covalency and the average force constant of the Er³⁺-oxygen bonds,

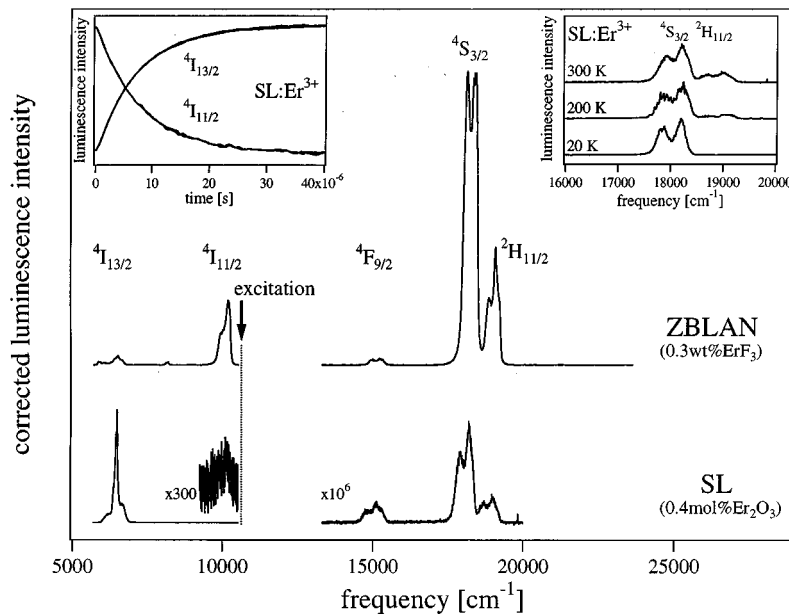


FIG. 3. Room-temperature luminescence spectra for a 0.4 mol % Er₂O₃-doped soda-lime-silicate glass (SL) (1.97 × 10²⁰ Er³⁺ cm⁻³) and a 0.3 wt % Er³⁺-doped ZBLAN fluoride glass (0.37 × 10²⁰ Er³⁺ cm⁻³) excited by the ⁴I_{15/2} → ⁴I_{11/2} transition around 980 nm. The multiplet terms indicate the initial state of the transition to the ⁴I_{15/2} ground-state multiplet. The spectra are corrected for absorbed power and plotted on the same normalized intensity scale. The equivalence of the ⁴I_{11/2} decay and the ⁴I_{13/2} rise for SL:0.4 mol % Er₂O₃ is shown in the left inset and the temperature dependence of upconversion luminescence from ⁴S_{3/2} and ²H_{11/2} in a SL:0.4 mol % Er₂O₃ is shown in the right inset.

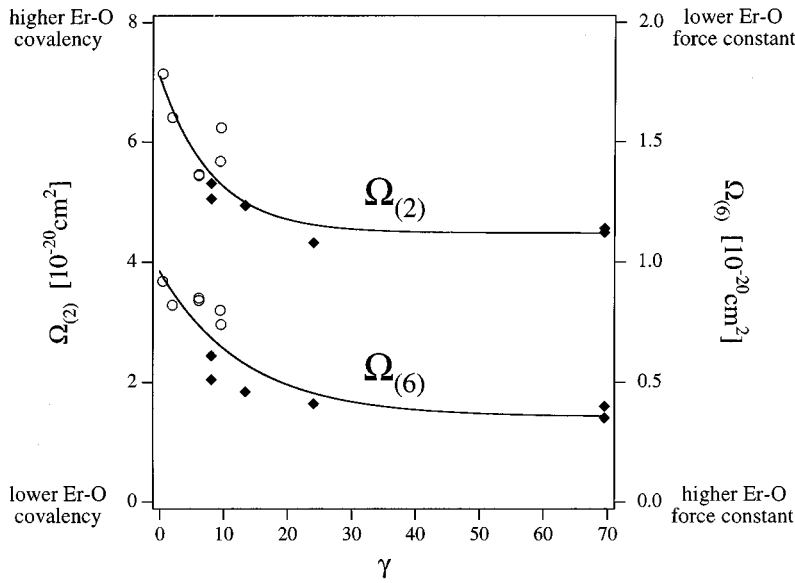


FIG. 4. $\Omega_{(2)}$ and $\Omega_{(6)}$ Judd-Ofelt intensity parameters of various 0.4 mol % Er_2O_3 -doped soda-lime-silicate (squares) and aluminosilicate (circles) glasses (from Table I) as a function of the ratio of nonbridging oxygen (NBO) vs total rare-earth (RE^{3+}) concentrations, γ . The curves are shown to guide the eye. Covalency and force constant of Er-O bonds are discussed in Sec. IV B and compared to the trend of the $\Omega_{(2)}$ and $\Omega_{(6)}$ parameter values.

respectively. The Judd-Ofelt model suggests an increasing covalency and a decreasing force constant of the Er^{3+} -oxygen bond upon lowering γ .

Figure 5 shows, for a variety of Er^{3+} -doped SL and AS glasses, the dependence of ${}^4I_{15/2} \rightarrow {}^4I_{13/2}$ oscillator strengths, f , obtained from room-temperature absorption spectra (see Fig. 2) on the ${}^4I_{13/2}$ relaxation rate constants, β , obtained from single-exponential fits to ${}^4I_{13/2} \rightarrow {}^4I_{15/2}$ room-temperature luminescence transients. The ${}^4I_{15/2} \rightarrow {}^4I_{13/2}$ oscillator strength for both SL (squares) and AS (circles) glasses is found to be a linear function of the ${}^4I_{13/2}$ relaxation rate constant. The intersection of the linear fit at the origin ($\beta_{f \rightarrow 0} = -3.1 \pm 5.1 \text{ s}^{-1}$) indicates the virtual absence of nonradiative processes from ${}^4I_{13/2}$ in the regime of low excitation densities used in this experiment.

The absolute ${}^4I_{13/2}$ luminescence quantum yield, η , is defined as the ratio of the number of photons emitted by the ${}^4I_{13/2} \rightarrow {}^4I_{15/2}$ ($\sim 1.55 \mu\text{m}$) transition and the number of pho-

tons absorbed at the excitation wavelength ($\sim 980 \text{ nm}$) at low excitation densities ($\leq 5 \text{ W/cm}^2$). Figures 6 and 7 show η for Er^{3+} -doped and $\text{Er}^{3+}, \text{Yb}^{3+}$ -codoped SL and AS glasses, respectively. For both glass types, the quantum yield is around 0.90 at low Er^{3+} concentrations and drops to about 0.65 at 1.2 mol % Er_2O_3 [Figs. 6(a) and 6(b)]. A much more pronounced drop, indicative of an additional quenching mechanism, is observed for a SL glass prepared with a high OH^- concentration ($255 \pm 15 \text{ ppm OH}^-$) [Fig. 6(c)].

Figure 7 compiles quantum yields for a variety of SL (squares) and AS (circles) glasses doped with 0.4 mol % Er_2O_3 and codoped with Yb_2O_3 . The dotted line is shown to guide the eye, and it defines three Yb^{3+} concentration regimes: the data suggest a high η for low Yb^{3+} concentration (regime i), a low η for intermediate Yb^{3+} concentration (regime ii), and a restored high value of η at high Yb^{3+} concentration (regime iii).

The control of atmospheric conditions during glass prepa-

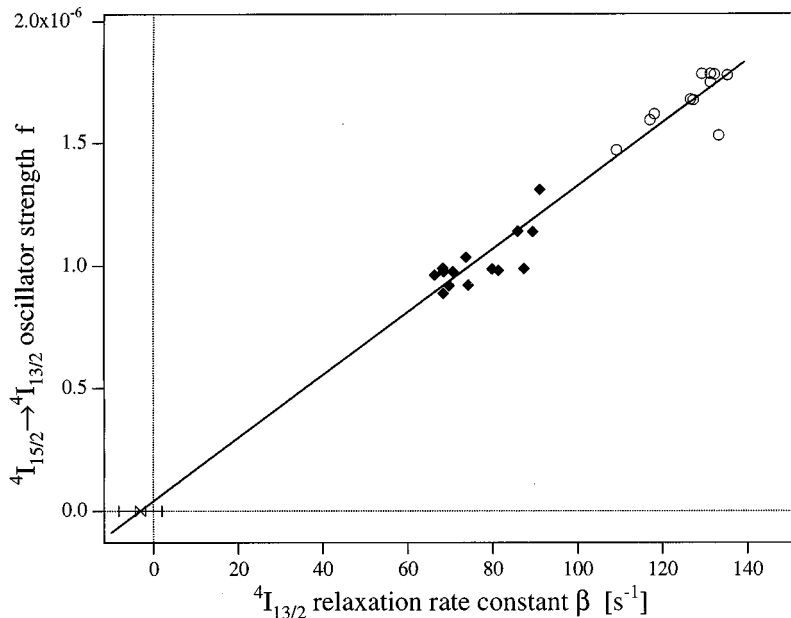


FIG. 5. ${}^4I_{15/2} \rightarrow {}^4I_{13/2}$ oscillator strengths, f , for soda-lime-silicate (squares) and aluminosilicate (circles) glasses as a function of room-temperature ${}^4I_{13/2}$ relaxation rate constants, β . The horizontal bar on the x axis indicates the standard deviation of the x intercept.

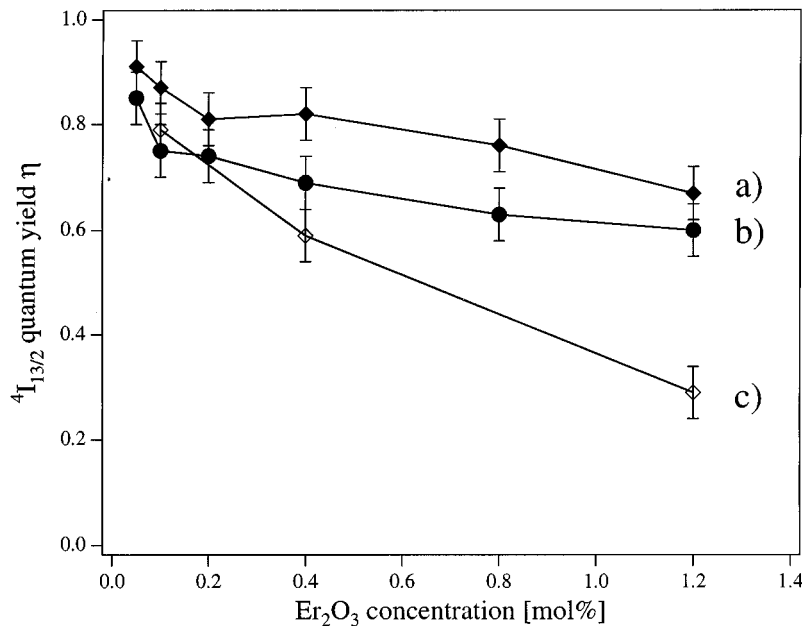


FIG. 6. Absolute $^4I_{13/2}$ luminescence quantum yields (for ~ 980 nm excitation) at room-temperature and low excitation density (≤ 5 W/cm²) for a concentration series of Er^{3+} -doped (a) soda-lime-silicate, (b) aluminosilicate, and (c) OH⁻ rich soda-lime-silicate (255 ± 15 ppm OH⁻) glasses.

ration allows for a tuning of the concentration of OH⁻ impurities in the samples. Figure 8 shows representative room-temperature midinfrared absorption spectra of the soda-lime-silicate and aluminosilicate glasses used in Fig. 6. The two peaks around 3500 and 2900 cm⁻¹, prominent in the OH⁻-rich SL sample, are assigned to fundamental $\equiv\text{SiO-H}$ vibrations in which the OH group is either free or engaged in hydrogen bonding with a neighboring nonbridging oxygen atom (NBO), respectively.¹⁶ Indicated OH⁻ concentrations therefore represent the sum of various types of Si-OH configurations and were calculated using the oscillator strength values derived by Scholtz.¹⁶ OH⁻ concentrations of 255 ± 15 ppm and $< 55 \pm 15$ ppm were estimated for the OH⁻-rich glasses and for the glasses prepared under dry atmosphere (< 1 ppm H₂O), respectively.

Upconversion luminescence spectra for several AS

glasses excited around 975 nm are shown in Fig. 9. The excitation density was 51 kW/cm² in the focal region, and the samples (~ 0.5 cm³) were at room temperature at the surface. Due to the small $^2H_{11/2} - ^4S_{3/2}$ energy separation, the $^2H_{11/2}$ excited state is easily thermally populated from $^4S_{3/2}$ and subsequently contributes to the radiative relaxation in this spectral range at room temperature (see right inset, Fig. 3). From bottom to top, a strong increase of the $^2H_{11/2} \rightarrow ^4I_{15/2}$ to $^4S_{3/2} \rightarrow ^4I_{15/2}$ intensity ratio is observed, indicating an increasing internal sample temperature T_i . This trend is correlated with an increasing absorption coefficient, $\alpha(\lambda_{\text{ex}})$, at the excitation wavelength, λ_{ex} , which was achieved by Yb³⁺ codotiation of the 0.4 mol % Er_2O_3 -doped glasses.

Figure 10 plots internal sample temperatures T_i calculated from upconversion luminescence spectra (as shown in Fig. 9)

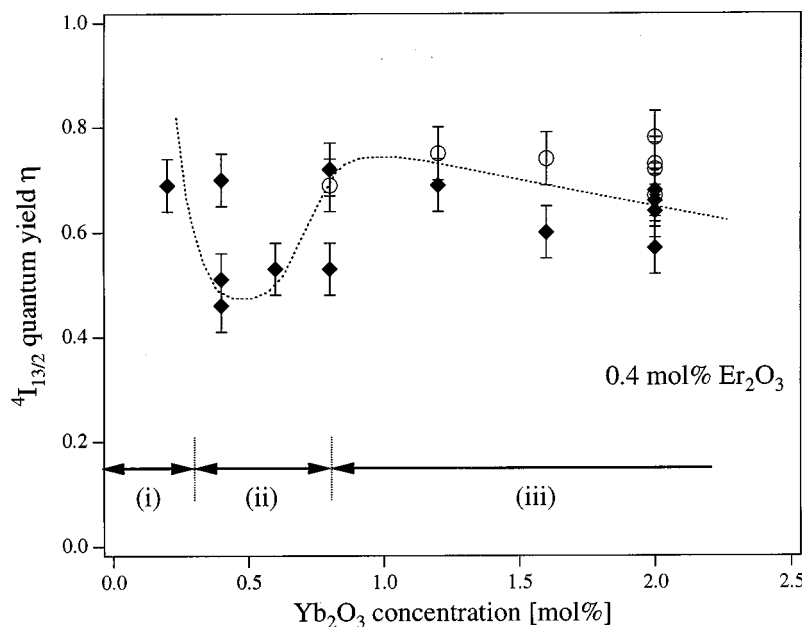


FIG. 7. Absolute $^4I_{13/2}$ luminescence quantum yields (for ~ 980 nm excitation) at room-temperature and low excitation density (≤ 5 W/cm²) for a concentration series of 0.4 mol % Er_2O_3 -doped soda-lime-silicate (squares) and aluminosilicate (circles) glasses codoped with Yb_2O_3 . The dotted line, shown to guide the eye, defines three Yb^{3+} concentration regimes discussed in Sec. IV D 2.

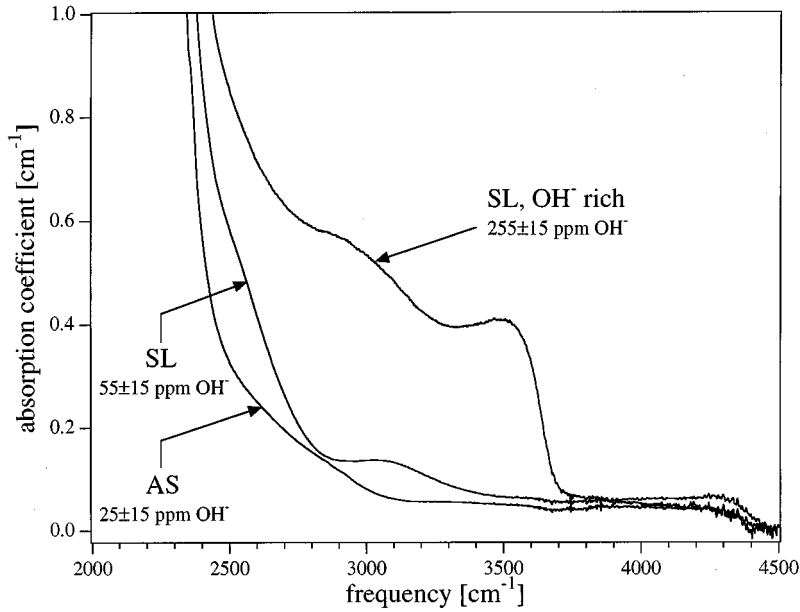


FIG. 8. Representative room-temperature midinfrared absorption spectra of the soda-lime-silicate (SL) and aluminosilicate (AS) glasses shown in Fig. 6. The two high-energy vibrational OH^- modes around 3500 cm^{-1} and 2900 cm^{-1} are prominent in the OH^- -rich sample and strongly suppressed in the samples prepared under dry air ($<1\text{ ppm H}_2\text{O}$).

as a function of the absorption coefficient at the excitation wavelength, $\alpha(\lambda_{\text{ex}})$, for a variety of 0.4 mol % Er_2O_3 -doped SL and AS glasses codoped with 0–4 mol % Yb_2O_3 . Within the accuracy of the data, SL (squares) and AS (circles) glasses exhibit the same behavior. As indicated by the almost linear dependence of T_i on $\alpha(\lambda_{\text{ex}})$, the involved transitions were not saturated at the 51-kW/cm^2 excitation intensity used for these experiments. Significant internal sample heating is *only* found for samples codoped with Yb^{3+} [$\alpha(\lambda_{\text{ex}}) > 0.5\text{ cm}^{-1}$], and the maximum internal sample temperature of 572 K is measured for a 0.4 mol % Er_2O_3 aluminosilicate codoped with 4 mol % Yb_2O_3 . The inset shows the ${}^2\text{H}_{11/2} \rightarrow {}^4\text{I}_{15/2}$ to ${}^4\text{S}_{3/2} \rightarrow {}^4\text{I}_{15/2}$ luminescence intensity ratio as a function of excitation wavelength in the region of the Yb^{3+} absorption (see Fig. 2) for a codoped aluminosilicate glass. The similarity of this curve and the corresponding Yb^{3+} absorption spectrum is another manifestation of the

correlation of internal temperature and absorption coefficient.

The temperature dependence of the ${}^4\text{I}_{13/2}$ lifetime in a 0.4 mol % Er_2O_3 -doped soda-lime-silicate glass is presented in Fig. 11. Only a slight drop from 13.8 to 11.4 ms is found upon increasing the sample temperature from 12 to 678 K . This decrease results from the shorter radiative lifetimes to be found in higher-lying crystal-field levels of the ${}^4\text{I}_{13/2}$ multiplet, and it is consistent with the multiphonon relaxation from the ${}^4\text{I}_{13/2}$ multiplet being negligible, even in the most strongly internally heated samples shown in Fig. 10.

IV. DISCUSSION

The present study focuses on the properties of excited states of Er^{3+} and Yb^{3+} with energies below 27000 cm^{-1} , i.e., on the visible and near-infrared spectral range, and the

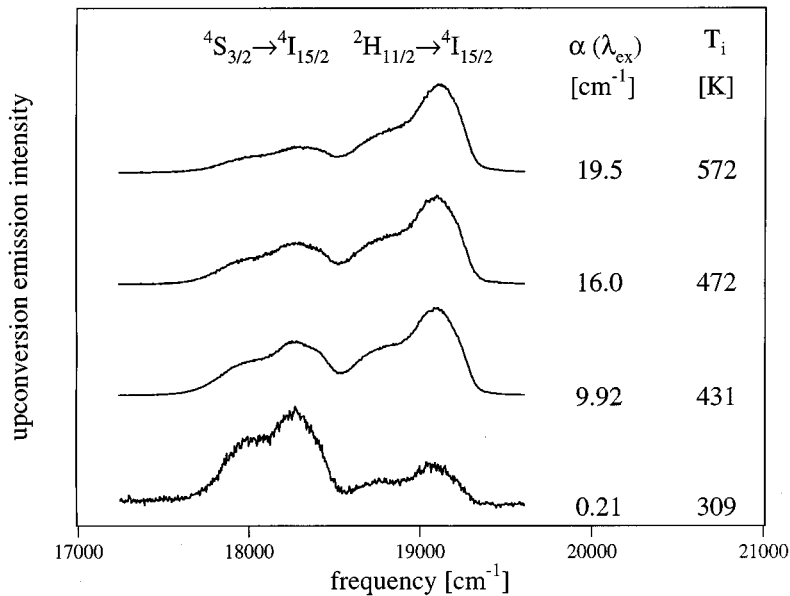


FIG. 9. Room-temperature upconversion luminescence spectra of several 0.4 mol % Er_2O_3 -doped aluminosilicate glasses codoped (except bottom sample) with Yb_2O_3 and excited around 975 nm with 51 kW/cm^2 . The absorption coefficient at the excitation wavelength, $\alpha(\lambda_{\text{ex}})$, and the calculated internal temperature, T_i (see Sec. IV D 3), are indicated.

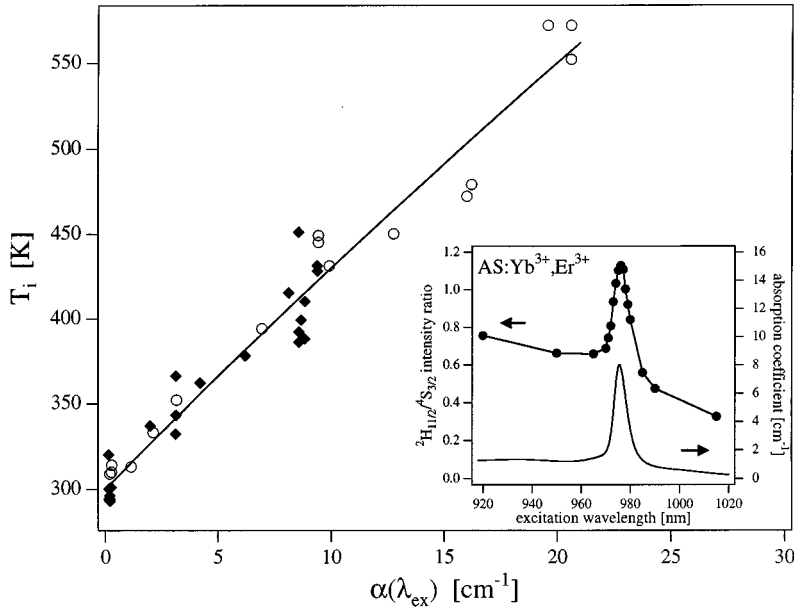


FIG. 10. Calculated [Eqs. (7) and (8)] internal sample temperatures T_i for a variety of 0.4 mol % Er_2O_3 -doped soda-lime-silicate (squares) and aluminosilicate (circles) codoped with 0–4 mol % Yb_2O_3 as a function of the absorption coefficient $\alpha(\lambda_{\text{ex}})$ at the excitation wavelength λ_{ex} . Glasses with $\alpha(\lambda_{\text{ex}}) > 0.5 \text{ cm}^{-1}$ correspond to samples codoped with Yb_2O_3 . The solid curve is a least-squares fit of Eq. (10) to the entire data set. The inset compares the ${}^2H_{11/2}/{}^4S_{3/2}$ upconversion intensity ratio (see Fig. 9) with the absorption coefficient as a function of the excitation wavelength in the ${}^2F_{7/2} \rightarrow {}^2F_{5/2}$ absorption region of a Yb^{3+} , Er^{3+} -codoped aluminosilicate glass.

respective $4f$ energy-level diagrams of both ions are schematically shown in Fig. 1. The transitions ${}^4I_{15/2} \rightarrow {}^4I_{11/2}$ and ${}^2F_{7/2} \rightarrow {}^2F_{5/2}$ were used to excite Er^{3+} and Yb^{3+} around 980 nm, respectively. Sections IV A–IV C first consider single-ion processes and discuss inhomogeneous broadening, radiative transitions, and multiphonon relaxation of Er^{3+} in various soda-lime-silicate (SL) and aluminosilicate (AS) glasses. Two-ion energy-transfer processes are subsequently introduced in Sec. IV D, where the role of Yb^{3+} as a sensitizer for Er^{3+} is analyzed.

A. Inhomogeneous broadening vs crystal-field splitting

The spectral structure of the Er^{3+} ${}^4I_{15/2} \leftrightarrow {}^4I_{13/2}$ transition is of particular interest for optical signal amplification around $1.55 \mu\text{m}$ since it determines both the number and the wavelength of channels which can be operated within the

${}^4I_{13/2} \rightarrow {}^4I_{15/2}$ gain profile in a POWA device. The disordered glass host offers a broad distribution of coordination sites for Er^{3+} and Yb^{3+} ions and, as a result, optical transitions are inhomogeneously broadened. In contrast to crystalline hosts, the absorption spectra in Fig. 2 therefore show little spectral structure.

In Fig. 2 it is evident that the various absorption transitions show more structure in SL glass than in AS glass. This is particularly obvious in the inset which presents the least (SL) and the most (AS) broadened ${}^4I_{15/2} \rightarrow {}^4I_{13/2}$ absorption spectrum in the glasses studied here. At a given temperature, the spectral profile of an optical transition $|SLJ\rangle \rightarrow |S'L'J'\rangle$ is determined by the crystal-field splittings of the respective multiplets, the oscillator strengths of the individual crystal-field transitions, the homogeneous broadening (e.g., thermal broadening), and the inhomogeneous broadening (mainly a result of short-range disorder in the host lattice). The inho-

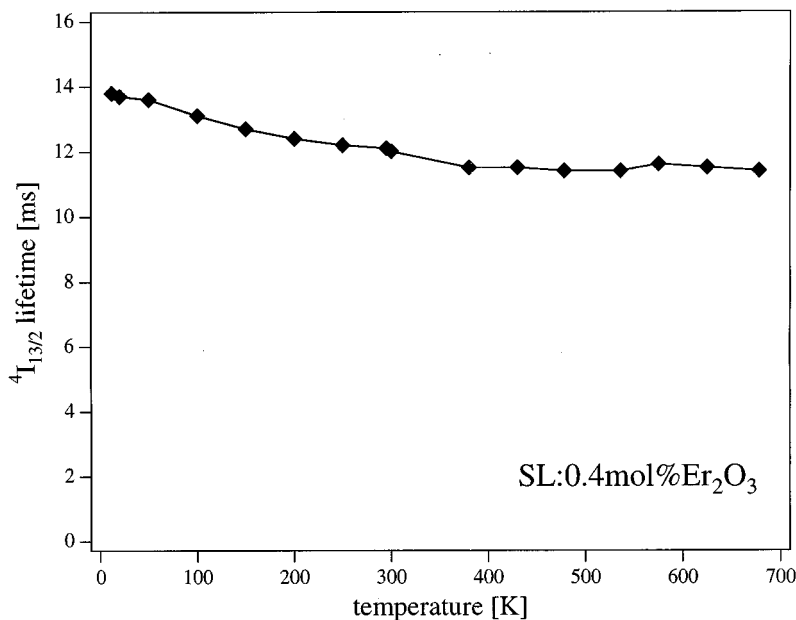


FIG. 11. Temperature dependence of the ${}^4I_{13/2}$ lifetime in a 0.4 mol % Er_2O_3 -doped soda-lime-silicate glass. The values were obtained from single-exponential fits to the $1.55\text{-}\mu\text{m}$ luminescence transients (not shown).

homogeneous broadening in rare-earth-doped crystalline hosts is typically much smaller than the overall crystal-field splitting of $^{2S+1}L_J$ multiplets, and the various peaks within a $|SLJ\rangle \rightarrow |S'L'J'\rangle$ transition usually correspond to individual (mainly homogeneously broadened) crystal-field transitions (see, e.g., the Y₂O₃:Er³⁺ spectrum in the inset of Fig. 2). In glasses, on the other hand, inhomogeneous broadening can, in principle, become comparable to or greater than the overall crystal-field splitting of the $^{2S+1}L_J$ multiplets. The $^4I_{15/2} \rightarrow ^4I_{13/2}$ absorption spectra (inset Fig. 2) provide information on the relative magnitude of the inhomogeneous width in the present SL and AS glasses. Although the width of the various features in the $^4I_{15/2} \rightarrow ^4I_{13/2}$ spectral profiles differs appreciably between SL and AS glasses, the five-peak structure as well as the total width of the transition is very similar. From the crystal-field splittings of $^4I_{15/2}$ and $^4I_{13/2}$ reported for the Er³⁺-doped oxide crystals YAG, YSAG, and YSGG,¹⁷ the total width of the $^4I_{15/2} \rightarrow ^4I_{13/2}$ transition is expected to be about 370–430 cm⁻¹ at room temperature. This value is in good agreement with the total width of about 280–350 cm⁻¹ which is spanned by the five peaks shown in Fig. 2. In addition, the $^4I_{15/2} \rightarrow ^4I_{13/2}$ absorption spectra of SL and AS glass show much similarity, in both the energy position and the relative intensity of the main features, with the room-temperature absorption spectrum of a 1% Er³⁺-doped Y₂O₃ crystal. For both SL and AS glass we therefore conclude that the inhomogeneous broadening of $^4I_{15/2} \leftrightarrow ^4I_{13/2}$ crystal-field transitions is bigger than the homogeneous broadening but still significantly smaller than the overall crystal-field splitting of these multiplets. The structure of the $^4I_{15/2} \leftrightarrow ^4I_{13/2}$ transition in both glasses is therefore mainly determined by the $^4I_{15/2}$ and $^4I_{13/2}$ crystal-field splittings, the latter being of slightly smaller magnitude compared to oxide crystals.

This conclusion defines the realizable wavelength range of 1.55- μ m signal amplification by Er³⁺. Since the $^4I_{13/2} \rightarrow ^4I_{15/2}$ luminescence range is determined by the crystal field, even in highly disordered glasses, the energy range in which useful gain can be achieved is about 6050 cm⁻¹ (1.65 μ m) to 6900 cm⁻¹ (1.45 μ m) (see Fig. 3). However, maximizing inhomogeneous broadening is essential for obtaining a smooth gain profile in this wavelength range. Section IV B provides a detailed analysis of the factors determining the magnitude of inhomogeneous broadening and of overall crystal-field splittings in the present glasses.

B. Judd-Ofelt analysis

Oscillator strengths obtained from room-temperature absorption spectra of Er³⁺-doped SL and AS glasses (see Fig. 2) were used as experimental input for a Judd-Ofelt intensity analysis. The Judd-Ofelt model describes the perturbation of the $4f^n$ states by opposite parity $4f^{n-1}nl$ (where nl is mainly $5d$) on the basis of three parameters $\Omega_{(\lambda)}$ ($\lambda = 2, 4, 6$).^{18–20} The model assumes the states of the perturbing $4f^{n-1}nl$ configurations to be degenerate and the energy difference between these perturbing states and all the states of the $4f^n$ configuration to be equal. The model further assumes an isotropic medium, equal frequencies of the crystal-field transitions within a $|SLJ\rangle \rightarrow |S'L'J'\rangle$ multiplet transition, and equal thermal population of the crystal-field levels

within the $|SLJ\rangle$ initial state. For rare-earth-doped glasses at room temperature these conditions are typically sufficiently well satisfied. The electric-dipole-induced oscillator strength, f_{ed} , of a transition $|SLJ\rangle \rightarrow |S'L'J'\rangle$ is then given by

$$f_{\text{ed}} = \frac{8\pi^2 m \nu}{3h} \frac{\chi_{\text{ed}}}{(2J+1)} \sum_{\lambda=2,4,6} \Omega_{(\lambda)} |\langle SLJ \| \mathbf{U}^{(\lambda)} \| S'L'J' \rangle|^2, \quad (1)$$

where m is the electron mass, ν is the frequency of the transition, and χ_{ed} is the electric-dipole local-field correction which is $(n^2+2)^2/9n$ and $n(n^2+2)^2/9$ for absorption and emission, respectively, with n being the sample refractive index. The reduced matrix element of the tensor operator $U^{(\lambda)}$ in Eq. (1) can be approximated on the basis of intermediate coupling $|SLJ\rangle$ wave functions, i.e., it includes the electronic repulsion parameters $F_{(k)}$ and the spin-orbit coupling constant ζ . For the following analysis of SL and AS glasses, these parameters have been estimated from correlation crystal-field calculations reported for several Er³⁺-doped oxide crystals,¹⁷ and the average values $F_{(2)} = 422.45$ cm⁻¹, $F_{(4)} = 65.05$ cm⁻¹, $F_{(6)} = 6.743$ cm⁻¹, $\zeta = 2371$ cm⁻¹ were assumed. (Note the conversion relations $F^{(2)} = 225 \cdot F_{(2)}$, $F^{(4)} = 1089 \cdot F_{(4)}$, and $F^{(6)} = (184041/25) \cdot F_{(6)}$.) The magnetic-dipole induced isotropic oscillator strength, f_{md} , which is nonzero for transitions with $\Delta J = 0, \pm 1$, is given by

$$f_{\text{md}} = \frac{8\pi^2 m \nu}{3he^2} \frac{\chi_{\text{md}}}{(2J+1)} |\mu_B|^2 |\langle SLJ \| \mathbf{L} + 2\mathbf{S} \| S'L'J' \rangle|^2, \quad (2)$$

where e is the electron charge, μ_B is the Bohr magneton, and χ_{md} is the magnetic-dipole local-field correction which is n and n^3 for absorption and emission, respectively. The $\Omega_{(\lambda)}$ parameters are obtained from intensity-weighted least-squares fitting of calculated total oscillator strengths $f^{i \rightarrow j} = f_{\text{ed}}^{i \rightarrow j} + f_{\text{md}}^{i \rightarrow j}$ [Eqs. (1) and (2)] to experimental oscillator strengths $f_{\text{expt}}^{i \rightarrow j}$. ($f_{\text{expt}}^{i \rightarrow j}$ is obtained by numerical integration of the $i \rightarrow j$ absorption [$\epsilon(\bar{\nu})$ in (l mol⁻¹ cm⁻¹) vs $\bar{\nu}$ in (cm⁻¹)] and conversion according to $f_{\text{expt}}^{i \rightarrow j} = 4.31907 \times 10^{-9}$ mol cm² l⁻¹ $\times \int_{i \rightarrow j} \epsilon(\bar{\nu}) d\bar{\nu}$.) The results for various Er³⁺-doped SL and AS glasses are summarized in Table I.

With the addition of glass modifiers (M^{n+}) such as Na⁺, Ca²⁺, Mg²⁺, or rare-earth (RE³⁺) ions, linkages in the [SiO₄] network of silica glass are broken. Consequently, there are bridging oxygen (BO) atoms and nonbridging oxygen (NBO) ions, the latter having a formal charge of -1 and being the only negatively charged species in the glass. In effect, the silica network becomes a polyanion with net negative charge primarily localized at NBO's. Charge balance is achieved with the presence of the constituent cations M^{n+} in interstitial sites. Depending on the structure of the network and on the size, charge, and field strengths of these cations, they will form associates with network oxygens with varying degrees of ionic/covalent character. As the number of NBO's per Si atom increases not only does the overall network attain (i) higher negative charge, (ii) higher probability of NBO's on adjacent Si atoms, and (iii) higher probability of multiple NBO's on any given Si atom but it can also (iv)

more easily undergo structural reorganization to accommodate cations in preferred coordinations. The addition of alumina adds another factor for it is expected to incorporate into the silica network in a tetrahedral coordination, eliminating one NBO. Consequently there will be a net negative charge associated with the aluminum site, spread over adjacent oxygens and beyond, which must also achieve charge compensation.

The following discussion is an attempt to extract information on the local interactions of Er^{3+} with the surrounding glass network as a function of glass composition from the Judd-Ofelt parameters $\Omega_{(2)}$ and $\Omega_{(6)}$ obtained from the absorption spectra. The $\Omega_{(2)}$ parameter was proposed to be a measure of the degree of covalency of the chemical bonds between RE^{3+} and its nearest-neighbor atoms.²¹ Typical $\Omega_{(2)}$ values for Er^{3+} systems range from 1×10^{-20} to $15 \times 10^{-20} \text{ cm}^2$, but values of up to $100 \times 10^{-20} \text{ cm}^2$ (for ErI_3) have been observed in highly covalently bonded Er^{3+} complexes in vapors.^{22,23} The $\Omega_{(2)}$ values derived from the spectral measurements for SL and AS glasses range from 4.32×10^{-20} to $7.14 \times 10^{-20} \text{ cm}^2$ (Table I), and a pronounced $\sim 60\%$ increase in the $\Omega_{(2)}$ values is observed upon lowering the NBO/ RE^{3+} concentration ratio, γ , from 69 to 0.5 (see Fig. 4). The $\Omega_{(6)}$ parameter was proposed to increase with decreasing ‘‘rigidity’’ of the medium,²¹ i.e., the mean force constant of the Er^{3+} -oxygen bonds in our context, and $\Omega_{(6)}$ values are usually higher for glasses than for crystals. As shown in Fig. 4, $\Omega_{(6)}$ exhibits a similar dependence as $\Omega_{(2)}$ on γ , significantly increasing as γ is lowered from 69 to 0.5. The Judd-Ofelt analysis therefore seems to indicate a higher covalency and a lower force constant of the Er^{3+} -oxygen bonds at low NBO/ RE^{3+} concentration ratios.

Since NBO's are bonded to only one Si atom and oxygen prefers a twofold coordination, part of the NBO excess charge will be donated to a coordinating RE^{3+} ion and form a RE^{3+} -O-Si bond with significant covalent character and structurally resembling the fundamental Si-O-Si linkage of the glass. A BO, on the other hand, engaged in a Si-O-Si linkage and coordinatively saturated, has donated most of its charge to the two Si atoms. A RE^{3+} ion coordinating to a BO therefore will receive little charge from the oxygen and thus form a RE^{3+} -OSi₂ bond which is more ionic than the RE^{3+} -NBO bond. Also, as a result of its higher degree of covalency and directionality, the RE^{3+} -NBO bond is expected to have a higher force constant. As the NBO/ RE^{3+} concentration ratio is compositionally lowered, RE^{3+} ions have to compete for preferred NBO coordination and an increasing number of RE^{3+} ions will be forced to coordinate to BO's. On average, a decrease of both the covalency and the force constant of the RE^{3+} -O bonds is therefore expected. This conclusion is in contradiction to the trend of $\Omega_{(2)}$ and in accordance with the trend of $\Omega_{(6)}$ shown in Fig. 4. This result raises two questions: (i) is the proposed dependence of $\Omega_{(2)}$ on the degree of covalency of the nearest-neighbor chemical bond²¹ universally valid and (ii) do the Judd-Ofelt parameters, which were derived from the absorption spectra of the bulk glasses, actually represent the correct average over the ensemble of all Er^{3+} -O bonds in the sample or are the parameters strongly determined by some specific Er^{3+} -O bonds having a behavior different from that of the ensemble average? We are unable to answer these questions without

substantiating evidence. Also we have not addressed the possible effect of Al incorporation and its associated negative charge. This will affect the nature of adjacent BO's and their ability to interact with nearby cations. Specific information on any idiosyncrasies of the structure of the RE^{3+} -doped aluminosilicate glasses which may affect the situation are also unavailable. Our analysis, although based on a considerable number of samples, illustrates some of the difficulties faced when trying to extract information on microscopic physical properties from the ‘‘bulk’’-type Judd-Ofelt parameters.

C. Multiphonon vs radiative relaxation

The high vibrational energies (up to $1000\text{--}1100 \text{ cm}^{-1}$) of the basic $[\text{SiO}_4]$ structural unit of SL and AS glasses make nonradiative relaxation of Er^{3+} excited states through multiphonon emission a highly probable process. The relative efficiencies of radiative and multiphonon relaxation to a large extent determine the intensity distribution of the luminescence spectrum. For most of the excited states, multiphonon relaxation is dominant, and, as shown in Fig. 3, luminescence from only a few states is observed. The multiphonon relaxation rate constant, k_{mp} , from a given excited state can be estimated from the energy-gap law. At 0 K, multiphonon relaxation is due to spontaneous phonon emission, and the respective rate constant is given by

$$k_{\text{mp}}(0) = \beta e^{-\alpha(\Delta E - 2\hbar\omega_{\text{max}})}, \quad (3)$$

where α and β are positive-definite constants characteristic of the host material, $\hbar\omega_{\text{max}}$ is the highest energy optical phonon, and ΔE is the energy difference between the relaxing and the next lower state.²⁴ With increasing temperature T , the stimulated emission of phonons by thermal phonons increases, and $k_{\text{mp}}(T)$ becomes

$$k_{\text{mp}}(T) = k_{\text{mp}}(0) \cdot [1 - e^{-\hbar\omega_{\text{max}}/kT}]^{-p}, \quad (4)$$

where $p = \Delta E/\hbar\omega_{\text{max}}$ is the minimum number of phonons required to bridge the energy gap ΔE .^{25,26} On the basis of Eq. (4), room-temperature multiphonon relaxation rate constants for the various Er^{3+} excited states can be estimated. In SL and AS glasses of compositions used here $\hbar\omega_{\text{max}}$ is 1100 and 1015 cm^{-1} , respectively,²⁷ and the parameters $\alpha = 4.7 \times 10^{-3} \text{ cm}^{-1}$ and $\beta = 9.0 \times 10^7 \text{ s}^{-1}$ reported for silica glass²⁴ were used for the calculation. Since the multiplet energies only change slightly between the two glass types, respective energy gaps (given in Table II) have been assumed equal. The spontaneous radiative relaxation rate constant k_r for a transition $j \rightarrow i$ is given by

$$k_r^{j \rightarrow i} = \frac{2\pi e^2}{\epsilon_0 m c^3} \cdot \nu^2 f_{j \rightarrow i} = \frac{2\pi e^2}{\epsilon_0 m c^3} \cdot n^2 \nu^2 f_{i \rightarrow j}, \quad (5)$$

where ϵ_0 is the vacuum permittivity and $f = f_{\text{ed}} + f_{\text{md}}$ is the total oscillator strength [Eqs. (1) and (2)]. Table II summarizes the calculated multiphonon relaxation rate constants [Eq. (5)] for the relevant excited-state multiplets of Er^{3+} . With the exception of ${}^4I_{13/2}$, multiphonon decay is the dominant relaxation process for all excited-state multiplets. The slightly lower maximum phonon energy of AS glass decreases $k_{\text{mp}}(T)$ by about a factor of 2.2 with respect to SL

TABLE II. Calculated radiative (k_r) [Eq. (5)] and multiphonon (k_{mp}) [Eq. (4)] relaxation rate constants (s^{-1}) and calculated radiative decay fractions [$r = k_r / (k_r + k_{mp})$] for the lowest $^{2S+1}L_J$ multiplets in 0.4 mol % Er₂O₃-doped soda-lime-silicate ($\gamma = 69.5$) and aluminosilicate ($\gamma = 0.50$) glass. k_r was calculated from the Judd-Ofelt intensity parameters given in Table I. k_{mp} was calculated using the parameters $\alpha = 4.7 \times 10^{-3}$ cm, $\beta = 9.0 \times 10^7$ s⁻¹, and $T = 300$ K. Respective energy gaps ΔE have been assumed equal for both glasses. The highest vibrational energy $\hbar \omega_{max}$ is 1100 cm⁻¹ and 1015 cm⁻¹ for soda-lime-silicate and aluminosilicate glass, respectively (Ref. 27). Measured total relaxation rate constants k_{expt} are shown for comparison.

$^{2S+1}L_J$	ΔE (cm ⁻¹)	Soda-lime-silicate glass				Aluminosilicate glass			
		k_r	k_{mp}	r	k_{expt}	k_r	k_{mp}	r	k_{expt}
$^4I_{13/2}$	6600	68	9.7×10^{-2}	0.9986	74.2	137	4.4×10^{-2}	0.9997	126.4
$^4I_{11/2}$	3650	72	9.9×10^4	0.0007	$\sim 1.3 \times 10^5$	172	4.6×10^4	0.0037	$\sim 1.3 \times 10^5$
$^4I_{9/2}$	2265	84	6.6×10^7	~ 0		206	3.0×10^7	~ 0	
$^4F_{9/2}$	2810	546	5.2×10^6	0.0001		1380	2.3×10^6	0.0006	
$^4S_{3/2}$	3000	393	2.1×10^6	0.0002		1280	9.6×10^5	0.0013	
$^2H_{11/2}$	900	5044	4.1×10^{10}	~ 0		9648	1.8×10^{10}	~ 0	
$^4F_{7/2}$	1280	1191	6.8×10^9	~ 0		3235	3.1×10^9	~ 0	

glass. In addition, the radiative decay rate constants are about a factor of 2.5 higher in AS glass due to the higher oscillator strengths, giving an overall increase of the radiative decay fraction r in AS relative to SL glass. The predicted dominance of radiative relaxation from $^4I_{13/2}$, which is confirmed by the SL:0.4 mol % Er₂O₃ luminescence spectrum shown in Fig. 3, is also reflected in Fig. 5. Assuming an averaged weighted $^4I_{13/2} \rightarrow ^4I_{15/2}$ transition energy of 6548 cm⁻¹ and an average refractive index of 1.574 for the samples shown in Fig. 5, a slope in the f vs $k_r^{j \rightarrow i}$ graph of 1.41×10^{-8} s is calculated from Eq. (5). The linear fit to the data in Fig. 5 yields a slope of $(1.29 \pm 0.06) \times 10^{-8}$ s in approximate agreement with the theoretical value. The measured relaxation rate constant, k_{expt} , is the sum of radiative ($k_r^{j \rightarrow i}$) and nonradiative relaxation rate constants, and $k_r^{j \rightarrow i}$ vanishes for the hypothetical case $f = 0$ [Eq. (5)]. Therefore, the x -axis intercept of the linear fit in Fig. 5 is a direct measure of nonradiative contributions to the $^4I_{13/2}$ decay. The intercept of -3.1 ± 5.1 s⁻¹ obtained from the fit clearly shows the absence of nonradiative relaxation from $^4I_{13/2}$ in this low excitation density regime, supporting the conclusions reached above.

The calculated radiative decay fractions, r (Table II), indicate that besides $^4I_{13/2}$, radiative decay from $^4I_{11/2}$, $^4F_{9/2}$, and $^4S_{3/2}$ should also be observable. This is confirmed in Fig. 3 where weak luminescence from $^4I_{11/2}$ and weak up-conversion luminescence from $^4F_{9/2}$ and $^4S_{3/2}$ is observed. Upconversion luminescence from $^2H_{11/2}$ is a result of thermal population of $^2H_{11/2}$ from $^4S_{3/2}$ at room temperature, and it is not present at low temperatures (see right inset, Fig. 3). The upconversion luminescence properties of these glasses will be discussed in Sec. IV D.

Er³⁺-based materials for 1.55- μ m optical amplification rely on the high radiative quantum yield from $^4I_{13/2}$ to produce net gain for the $^4I_{13/2} \rightarrow ^4I_{15/2}$ transition. For that purpose, the $^4I_{13/2}$ state can, in principle, be directly excited. However, excitation of the $^4I_{11/2}$ state around 980 nm by powerful semiconductor diode lasers is also a practical excitation scheme, and in addition it allows for inversion of the $^4I_{15/2}$ and $^4I_{13/2}$ populations. From the above considerations

it is evident that $^4I_{11/2}$ excitation is very efficient in populating the $^4I_{13/2}$ excited-state multiplet in silica-based glasses. The left inset in Fig. 3 illustrates the correlation between the fast decay of the $^4I_{11/2}$ population (~ 7.8 μ s) and the rise of the $^4I_{13/2}$ population. However, this excitation scheme is not appropriate for all materials since the overall efficiency strongly depends on the relative magnitude of multiphonon and radiative relaxation rate constants. Requiring the $^4I_{13/2}$ luminescence quantum yield for $^4I_{11/2}$ excitation (η) to be ≥ 0.5 [i.e., $\eta_{11/2} < (1 - \sqrt{1/2})$ and $\eta_{13/2} > \sqrt{1/2}$] and assuming $\hbar \omega_{max} \geq kT$, the $\hbar \omega_{max}$ criterion

$$\frac{1}{2\alpha} \ln \left[\frac{k_{11/2}^r}{\beta(\sqrt{2}-1)} \right] + \frac{1}{2} \Delta E_{11/2} < \hbar \omega_{max}$$

$$< \frac{1}{2\alpha} \ln \left[\frac{k_{13/2}^r(\sqrt{2}-1)}{\beta} \right] + \frac{1}{2} \Delta E_{13/2} \quad (6)$$

follows from Eq. (4), where $k_{11/2}^r$ and $k_{13/2}^r$ are the radiative relaxation rate constants and $\Delta E_{11/2}$ and $\Delta E_{13/2}$ are the energy gaps for the $^4I_{11/2}$ and $^4I_{13/2}$ excited-state multiplets, respectively. Using typical parameter values for Er³⁺ in various hosts (see Ref. 24 and Table II), the criterion Eq. (6) precludes use of the $^4I_{11/2}$ excitation scheme for basically all the low-phonon halide materials such as fluorides, chlorides, or bromides. Evidence for this is the long, radiatively dominated $^4I_{11/2}$ lifetimes of 12.8, 11.0, and 3.75 ms observed in CsCdBr₃,²⁸ Cs₃Lu₂Br₉,²⁹ and YLiF₄,¹⁴ respectively. The luminescence spectrum of ZBLAN:Er³⁺, which shows a high relative $^4I_{11/2}$ luminescence intensity (Fig. 3), also confirms the $\hbar \omega_{max}$ criterion Eq. (6). Most oxide crystals and glasses, on the other hand, which span a range of $\hbar \omega_{max}$ from approximately 550 to 1400 cm⁻¹,²⁴ are optimum in this respect.

For silica-based glasses, Eq. (6) predicts the approximate range $480 < \hbar \omega_{max} < 1750$ cm⁻¹ (with $\hbar \omega_{max}$ actually being around 1000–1100 cm⁻¹) to provide a high $^4I_{13/2}$ luminescence quantum yield for $^4I_{11/2}$ excitation. The effect of optical phonons with energies above the 1750 cm⁻¹ upper limit can be seen in the $^4I_{13/2}$ luminescence quantum yield mea-

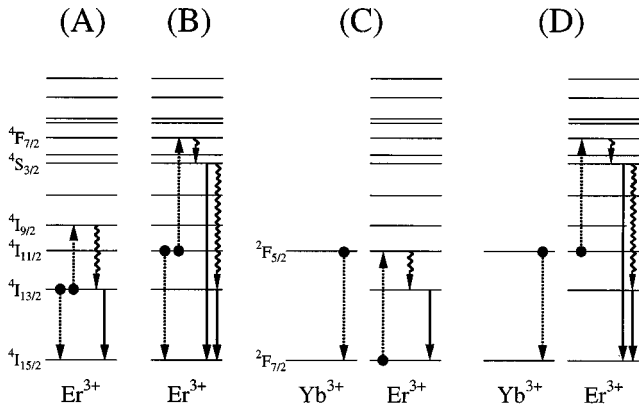


FIG. 12. Schematic representation of upconversion processes involving (a) two Er³⁺ ions in the $^4I_{13/2}$ excited-state multiplet, and (b) two Er³⁺ ions in the $^4I_{11/2}$ excited-state multiplet. (c) and (d) are Yb³⁺→Er³⁺ energy-transfer processes. Dotted, wiggly, and solid arrows indicate energy-transfer, multiphonon, and radiative processes, respectively.

surements (Fig. 6). The pronounced drop of η with increasing Er³⁺ concentration in a series of OH⁻-rich SL glasses (255 ± 15 ppm OH⁻) [Fig. 6(c)] is not observed in the low OH⁻ (<55 ppm OH⁻) glasses [Figs. 6(a) and 6(b)], and it indicates the presence of an additional nonradiative relaxation pathway. Energies around 3500 and 2900 cm⁻¹ are measured for the highest-energy vibrational modes of OH⁻ in these glasses (Fig. 8), in agreement with earlier vibrational studies.¹⁶ Some of the Er³⁺ ions will coordinate at these OH⁻ impurity sites.³⁰ Using Eq. (4) with the parameter values given in Table II, $^4I_{13/2}$ multiphonon relaxation rate constants of $\sim 2 \times 10^6$ s⁻¹ and $\sim 6 \times 10^8$ s⁻¹ are calculated for these two vibrational energies, respectively, indicating that $^4I_{13/2}$ luminescence of OH⁻-coordinated Er³⁺ ions will be completely quenched by multiphonon relaxation. Although this process is only active for a minority of Er³⁺ ions it becomes important at higher Er³⁺ concentrations. Above ~ 0.2 mol % Er₂O₃, energy migration of $^4I_{13/2}$ excitation through the Er³⁺ sublattice becomes efficient. As a result, Er³⁺-OH⁻ sites can be accessed and act as effective traps for $^4I_{13/2}$ excitation, significantly lowering the overall luminescence quantum yield for this state [Fig. 6(c)]. The OH⁻ impurity concentration is therefore one of the essential parameters in the preparation of Er³⁺-doped glasses for 1.55- μ m POWA devices.

D. Two-ion energy-transfer processes

1. Upconversion in Er³⁺-doped and Er³⁺, Yb³⁺-codoped glasses

At elevated Er³⁺ concentrations two-ion energy-transfer processes such as energy migration and upconversion become important and lead to additional nonradiative processes. One of the results of two-ion processes is a decreasing $^4I_{13/2}$ luminescence quantum yield with increasing Er³⁺ concentration [see Figs. 6(a) and 6(b)]. A variety of upconversion mechanisms are known for Er³⁺ systems. However, the dominance of multiphonon relaxation for most excited states in the present silica-based glasses (Sec. IV C) provides a considerable simplification of the excited-state dynamics.

For the following discussion of two-ion energy-transfer processes, we use the notation $(a_i, b_i) \rightarrow (a_f, b_f)$ where i and f represent initial and final states of two neighboring ions a and b . As schematically shown in Fig. 12, two energy-transfer upconversion processes are most likely to occur in the Er³⁺-doped silica glasses: $(^4I_{13/2}, ^4I_{13/2}) \rightarrow (^4I_{15/2}, ^4I_{9/2})$ (process A) and $(^4I_{11/2}, ^4I_{11/2}) \rightarrow (^4I_{15/2}, ^4F_{7/2})$ (process B). An additional energy-transfer mechanism exists in Er³⁺ samples codoped with Yb³⁺. The Yb³⁺ ion, with its excited-state multiplet $^2F_{5/2}$ having an energy comparable to $^4I_{11/2}$ (Er³⁺), can act as a sensitizer for Er³⁺ and transfer its energy to an unexcited Er³⁺ ion through the $(^4I_{15/2}, ^2F_{5/2}) \rightarrow (^4I_{11/2}, ^2F_{7/2})$ energy transfer (process C). The observed strong increase in intensity of all Er³⁺ luminescence transitions upon codotation with Yb³⁺ reflects the high efficiency of the Yb³⁺→Er³⁺ energy transfer at low excitation densities. It is well established that this first Yb→Er energy transfer may be followed by a second energy-transfer step (process D) from Yb³⁺ within the Er³⁺ $^4I_{11/2}$ lifetime, leading to the population of the $^4F_{7/2}$ (Er³⁺) multiplet through the process $(^4I_{11/2}, ^2F_{5/2}) \rightarrow (^4F_{7/2}, ^2F_{7/2})$ and subsequent upconversion luminescence.¹³

On the basis of excited-state lifetimes, relative efficiencies of the upconversion processes A, B, and C can be estimated. The long $^4I_{13/2}$ lifetimes, ranging from 7.5 to 14.7 ms in the materials studied here, make $(^4I_{13/2}, ^4I_{13/2}) \rightarrow (^4I_{15/2}, ^4I_{9/2})$ upconversion (process A) a very likely process. The relatively small exothermic energy mismatch of ~ 530 cm⁻¹ for process A matches the energy of Si-O-Si delocalized vibrational modes (400–700 cm⁻¹) (Refs. 31–33) which may enable a phonon-assisted energy transfer. However, no direct evidence of process A can be seen in the luminescence spectra (Fig. 3) since the $^4I_{9/2}$ multiplet, which is populated by this energy transfer, is efficiently quenched by multiphonon relaxation at all temperatures (Table II). On the other hand, luminescence from $^4S_{3/2}$, which is populated by multiphonon relaxation from $^4F_{7/2}$, is evidence for the activity of process B in the Er³⁺-doped samples. The short 7.8- μ s lifetime of the $^4I_{11/2}$ initial state of this process in combination with a high multiphonon relaxation rate constant from $^4S_{3/2}$ (Table II) leads to a low intensity of upconversion luminescence. The considerably longer lifetime of $^2F_{5/2}$ (Yb³⁺), 244 μ s in SL:0.2 mol % Yb₂O₃, strongly enhances the probability of processes B and D in the Er³⁺, Yb³⁺-codoped samples. However, on the basis of the present data, it is not possible to determine whether the strong intensity increase of upconversion luminescence upon Yb³⁺ codotation is a result of process B, process D, or a combination of both. Note that, in principle, the $^4S_{3/2}$ multiplet can also be reached by the interaction of three Er³⁺ ions in the $^4I_{13/2}$ multiplet, i.e., $(^4I_{13/2}, ^4I_{13/2}, ^4I_{13/2}) \rightarrow (^4I_{15/2}, ^4I_{15/2}, ^4S_{3/2})$. In spite of the long $^4I_{13/2}$ lifetime, this energy transfer process is expected to be significantly less probable than processes B or D at low excitation densities because it requires three steps with one of them involving the short-lived $^4I_{9/2}$ (see Table II) as an intermediate state. In fact, the decay of the $^4I_{13/2}$ excited-state multiplet under high $^4I_{11/2}$ excitation densities was found to be consistent with process A and did not reveal any three-ion interactions.³⁴

2. Yb³⁺ sensitization of Er³⁺

The efficiency of Yb³⁺ as a sensitizer for ⁴I_{13/2} (Er³⁺) luminescence depends on three factors: the rate of energy migration of ²F_{5/2} excitation among the Yb³⁺ ions, the Yb³⁺ → Er³⁺ energy-transfer rate (as well as the backtransfer rate), and the rate of multiphonon relaxation from ⁴I_{11/2} to ⁴I_{13/2} (Sec. IV C). Whereas the efficiencies of the Yb³⁺ → Er³⁺ energy transfer and the multiphonon relaxation step are mainly determined by the energy-level structure of Yb³⁺ and Er³⁺ ions and the phonon structure of the host, the efficiency of energy migration in the Yb³⁺ sublattice is primarily a function of the Yb³⁺ ion density. The absolute ⁴I_{13/2} luminescence quantum yields η of a concentration series of codoped samples provide quantitative guidelines for the optimization of Yb³⁺ sensitization of Er³⁺. The following discussion uses average ion separations calculated from the respective ion densities. In contrast to high silica glasses in which there is a limited solubility for rare-earth ions and thus a significant probability for ion clustering at high dopant levels, the solubility for rare-earth ions is much greater in the present SL and AS glasses, and the ion densities are well below the solubility limit. In fact, no evidence for Er³⁺ ion clustering in these glasses was found from time-resolved ⁴I_{13/2} upconversion studies, the respective ⁴I_{13/2} excited-state population dynamics being in exact agreement with a homogeneous two-ion upconversion process.³⁴ Therefore, a random distribution of RE³⁺ ions is assumed. As shown in Fig. 7, three Yb₂O₃ concentration regimes for fixed 0.4 mol % Er₂O₃ ($\sim 2 \times 10^{20}$ ions cm⁻³) can be defined: (i) at Yb₂O₃ concentrations below 0.3 mol % a significant fraction of the total absorption occurs on Er³⁺, which also absorbs at this wavelength and exhibits a high quantum yield at 0.4 mol % Er₂O₃ [Figs. 6(a) and 6(b)]. The large Yb³⁺-Yb³⁺ average distance of >19 Å in this regime prevents efficient migration of the fraction of excitation created on Yb³⁺, and therefore the ²F_{5/2} excited-state population decays mainly radiatively on Yb³⁺ rather than through energy transfer to Er³⁺. The sensitization by Yb³⁺ is therefore inefficient in this concentration regime, and the net result is a quantum yield which, due to the loss of the excitation created on Yb³⁺, is $\sim 25\%$ lower than the intrinsic value for 0.4 mol % Er₂O₃ (Fig. 6). In the intermediate regime (ii) of Yb₂O₃ concentrations in the range 0.4–0.8 mol %, the Yb³⁺-Yb³⁺ average distance is 17–14 Å and energy migration is still inefficient. Since the absorption coefficient of the ²F_{7/2} → ²F_{5/2} (Yb³⁺) transition is more than an order of magnitude higher than the absorption coefficient of the ⁴I_{15/2} → ⁴I_{11/2} (Er³⁺) transition at the excitation wavelength (see Fig. 2), a significant fraction of the total absorption now occurs on Yb³⁺. In combination with the inefficient energy migration this leads to a degradation of the ⁴I_{13/2} quantum yield which is almost half the intrinsic value for 0.4 mol % Er₂O₃. For Yb₂O₃ concentrations >0.8 mol % in regime (iii), the Yb³⁺-Yb³⁺ average distance is <14 Å, an ion separation for which resonant electric-multipole induced energy transfer typically becomes efficient.³⁵ Excitation created on Yb³⁺ can therefore migrate through other Yb³⁺ ions to unexcited Er³⁺ ions, which act as an efficient trap and subsequently emit from their ⁴I_{13/2} state. Sensitization of Er³⁺ by Yb³⁺ is operative in this regime, and the ⁴I_{13/2} quantum yield is restored to a

high value. The total ⁴I_{13/2} emission rate from the sample is given by the product of η times the total absorption rate. The best sample ($\eta = 0.78$, 2 mol % Yb₂O₃) shown in Fig. 7 absorbs about a factor of 80 stronger than a typical nonsensitized 0.4 mol % Er₂O₃ sample ($\eta \approx 0.8$). We conclude that, at excitation densities low enough to avoid saturation of the ⁴I_{13/2} population, the ⁴I_{13/2} excited-state population density can be enhanced by almost two orders of magnitude by codotation of 1–2 mol % Yb₂O₃ of a 0.4 mol % Er₂O₃ glass sample. This result is of importance to Er³⁺-based 1.55- μ m optical amplifiers since the small-signal gain for this transition depends exponentially on the population difference of the ⁴I_{13/2} and ⁴I_{15/2} multiplets.

3. Internal sample heating

As described above, near-infrared absorption (around 980 nm) in codoped samples is strongly enhanced by Yb³⁺. A particularly pronounced dependence of the relative upconversion luminescence intensities from the Er³⁺ ²H_{11/2} and ⁴S_{3/2} multiplets on the Yb³⁺ concentration and thus on the absorption coefficient at the excitation wavelength is observed in the glasses (see Fig. 9), indicating a significant internal heating of the Yb³⁺, Er³⁺-codoped samples. The inset in Fig. 10 also illustrates this direct correlation between the near-infrared absorption coefficient and the ²H_{11/2}:⁴S_{3/2} upconversion intensity ratio. The two multiplets ²H_{11/2} and ⁴S_{3/2} are separated by only several hundred wave numbers, and population in these two states can be treated as a closed system in thermal equilibrium.^{36,37} The luminescence intensity I of a subset of identical Er³⁺ ions is given by both the Boltzmann population of the individual crystal-field levels of ⁴S_{3/2} and ²H_{11/2} and by the oscillator strengths of the radiative transitions to the ⁴I_{15/2} ground-state multiplet. The luminescence intensity from crystal-field level i can thus be written as

$$I_{(i)} \propto \frac{g_i e^{-\Delta E_i/kT}}{\sum_j g_j e^{-\Delta E_j/kT}} \cdot \frac{f_i}{\sum_j f_j}, \quad (7)$$

where ΔE_i is the energy of the crystal-field level i relative to the lowest ⁴S_{3/2} crystal-field level, f_i is the sum of oscillator strengths from crystal-field level i to all crystal-field levels of the ⁴I_{15/2} ground-state multiplet, T is the temperature, g_i is the M_J degeneracy of the crystal-field level i (assumed 2 for Er³⁺ in the low site symmetries in the glass host), and j runs from 0 to 7 for the total of eight crystal-field levels of ⁴S_{3/2} and ²H_{11/2}. The relative ²H_{11/2}:⁴S_{3/2} luminescence intensity ratio is defined as

$$\frac{I(^2H_{11/2})}{I(^4S_{3/2})} = \frac{\sum_{j=2}^7 I(j)}{\sum_{j=0}^1 I(j)}. \quad (8)$$

Equation (8) can be used to obtain the internal sample temperature T_i from an experimental ²H_{11/2}:⁴S_{3/2} luminescence intensity ratio. There are two complications in the application of this model to the present silica glasses: (i) not all Er³⁺ ions are equivalent, i.e., the energy distribution of each ΔE_i is widened by inhomogeneous broadening, and (ii) the oscillator strengths of the individual (radiative) crystal-field transitions to the ⁴I_{15/2} ground-state are unknown. As illustrated by the inset in Fig. 2 and concluded in Sec. IV A, crystal-

field contributions dominate the spectral profile of the various transitions of Er^{3+} in SL and AS glasses and, moreover, the comparison with the oxide crystal $\text{Y}_2\text{O}_3:\text{Er}^{3+}$ revealed the good correspondence of relative intensities. With the assumption that an Er^{3+} -doped oxide crystal is adequate for modeling the thermal population of ${}^4S_{3/2}$ and ${}^2H_{11/2}$ in the present oxide glasses, we can take advantage of the detailed crystal-field analysis available for Er^{3+} -doped garnets. Gruber *et al.* used 117 crystal-field levels of the crystalline system $\text{Y}_3\text{Al}_5\text{O}_{12}:\text{Er}^{3+}$ (YAG: Er^{3+}) to describe the energy-level structure (between 0 and 43 465 cm^{-1} with a standard deviation of 13.20 cm^{-1}) by a Hamiltonian including a variety of first- and second-order atomic and crystal-field interactions.¹⁷ Note that by assuming the YAG: Er^{3+} atomic and

crystal-field parameters to be representative for all the SL and AS glasses in this study, the treatment presented below, for example, cannot account for changes in the oscillator strength of the hypersensitive ${}^4I_{15/2} \leftrightarrow {}^2H_{11/2}$ transition induced by small changes in the local Er^{3+} coordination geometry as the glass composition is varied. This problem, however, cannot be overcome unless the atomic and crystal-field parameters of each individual glass are known. Using the $|SLJM_J\rangle$ wave functions from Ref. 17 in combination with an electrostatic lattice sum calculation, which derives intensity parameters from the crystallographic structure and the isotropic oxide ion polarizability,³⁸ the relative oscillator strengths f_i defined in Eq. (7) can be calculated for YAG: Er^{3+} giving

f_i	${}^4S_{3/2}(i) \rightarrow$			${}^2H_{11/2}(i) \rightarrow$				
	$i=0$	1	2	3	4	5	6	7
$\rightarrow {}^4I_{15/2}(0-7)$	0.034	0.032	0.157	0.146	0.129	0.155	0.203	0.142
$\Sigma_i f_i$	0.066			0.934				

The ${}^4S_{3/2} : {}^2H_{11/2}$ total oscillator-strength ratio of 1:14.2 for transitions to ${}^4I_{15/2}$ predicted from this YAG: Er^{3+} calculation is in good agreement with the average ratios of 1:13 (as determined from the Judd-Ofelt calculations) and 1:18 (as determined from the measured absorption spectra), which supports the approach of using YAG: Er^{3+} as a model system for this calculation. The T_i vs $I({}^2H_{11/2}) : I({}^4S_{3/2})$ function obtained from applying this result in Eqs. (7) and (8) was therefore used to convert the experimental upconversion luminescence intensity ratios to internal sample temperatures T_i . This treatment improves over previous work³⁷ which neglected the crystal-field splitting of ${}^4S_{3/2}$ and ${}^2H_{11/2}$ and only considered a two-level system. Figure 10 shows the internal sample temperatures obtained from the experimental upconversion luminescence spectra as a function of the absorption coefficient at the excitation wavelength, $\alpha(\lambda_{\text{ex}})$, for SL and AS glasses with fixed 0.4 mol % Er_2O_3 concentration and codoped with 0–4 mol % Yb_2O_3 . Significant heating, of up to 572 K (299 °C) in some samples, is found for strongly absorbing glasses, i.e., for samples codoped with Yb^{3+} . The almost linear dependence of T_i on $\alpha(\lambda_{\text{ex}})$ indicates an excitation regime well below saturation for these experiments. Figure 11 shows that the ${}^4I_{13/2}$ lifetime remains almost constant at elevated temperatures. Therefore, the pronounced heating does not significantly affect the ${}^4I_{13/2}$ multiphonon relaxation rate constant, a behavior which is expected from Eq. (4) since thermal population of high-energy ($\hbar\omega_{\text{max}} \approx 1000\text{--}1100 \text{ cm}^{-1}$) phonons is still negligible in the entire range of internal sample temperatures reported in Fig. 10. As a result, thermomechanical, rather than spectroscopic, properties are expected to become relevant in the design of thin-film devices using strongly pumped Yb^{3+} -codoped glasses.

The sample heating is a result of multiphonon relaxation on Er^{3+} in the material. For Yb^{3+} , multiphonon relaxation is completely suppressed due to the large ${}^2F_{5/2} - {}^2F_{7/2}$ energy gap (see Fig. 1), and the ${}^2F_{5/2}$ excited-state multiplet either

decays radiatively or by energy transfer to ${}^4I_{11/2}$ (Er^{3+}). Most of this ${}^4I_{11/2}$ population on Er^{3+} efficiently decays to ${}^4I_{13/2}$ releasing 36% of the ${}^4I_{11/2}$ energy as phonons into the host lattice (Sec. IV C), with the respective phonon emission rate being a linear function of the absorbed power for low excitation densities. By treating the resulting increase of the internal sample temperature on the basis of the one-dimensional heat equation

$$T(r) = T(0) + \frac{P_{\text{diss}}}{4\pi r_0^2 l K} (r_0^2 - r^2), \quad (9)$$

where $T(r)$ is the temperature at a given radius, and P_{diss} is the dissipated phonon power in the cylinder of volume $\pi r_0^2 l$, an average thermal conductivity, K , can be estimated for the glasses shown in Fig. 10. Assuming the internal temperatures T_i calculated above to represent the maximum temperatures in the focal region, and assuming the spatial intensity distribution of the laser to be transversally uniform over a radius r_0 , it follows from Eq. (9) that

$$T_i = T_0 + \frac{\vartheta P(\lambda_{\text{ex}})}{4} \cdot \frac{r_0^2}{K} \cdot \left(\frac{1 - e^{-\alpha(\lambda_{\text{ex}})l}}{l} \right), \quad (10)$$

where ϑ is the fraction of the ${}^4I_{11/2}$ energy dissipated as phonons, T_0 is the external reference temperature, and $P(\lambda_{\text{ex}})$ and $\alpha(\lambda_{\text{ex}})$ are the excitation intensity and the absorption coefficient at wavelength λ_{ex} , respectively. Figure 10 shows a fit of Eq. (10) to the internal sample temperatures calculated above using $\vartheta = 0.36$, $P(\lambda_{\text{ex}}) = 51 \text{ kW/cm}^2$, and both r_0^2/K and l as parameters. The value of r_0 is not exactly known in our experiment. However, with the focal region 1.0–1.5 mm behind the sample front surface for all measurements shown in Fig. 10 and $r_0^2/K = 2.9 \times 10^{-5} \text{ m}^3 \text{ K W}^{-1}$ from the fit [Eq. (10)], the thermal conductivity is estimated to be between 3.5×10^{-2} and $7.7 \times 10^{-2} \text{ W m}^{-1} \text{ K}^{-1}$, in

good agreement with the known value for soda-lime-silicate glass of $4.8 \times 10^{-2} \text{ W m}^{-1} \text{ K}^{-1}$.³⁹

V. CONCLUSIONS

From a spectroscopic study of an extensive series of Er³⁺-doped and Yb³⁺,Er³⁺-codoped soda-lime-silicate (SL) and aluminosilicate (AS) glasses it is found that multiphonon relaxation from the ⁴I_{13/2} (Er³⁺) excited state is absent in both glass types, and that AS glasses, relative to SL glasses, generally exhibit higher oscillator strengths and larger inhomogeneous broadening of the 4f transitions as well as a smaller overall crystal-field splitting of the ^{2S+1}L_J multiplets. The Er³⁺-doped AS glasses studied here therefore not only show a favorable smoothing of the Er³⁺ ⁴I_{13/2}→⁴I_{15/2} gain profile at 1.55 μm but also a pronounced increase of the respective radiative relaxation rate constant and hence potential gain in an optical amplifier device. Although the Judd-Ofelt model is able to provide a phenomenological description of the 4f transition intensities on a quantitative basis it was not successful in reproducing the overall trend in the covalency of the Er³⁺-oxygen bond expected from structural considerations. Substantiating structural and spectroscopic evidence is required to fully understand the observed trends in the Ω_(λ) intensity parameters. From absolute ⁴I_{13/2} luminescence quantum yield measurements it is further concluded that a minimum of ~0.8 mol % Yb₂O₃ codotation is required in 0.4 mol % Er₂O₃ samples to achieve a suffi-

ciently large diffusion length for the ²F_{5/2} excitation and thus efficient sensitization of Er³⁺ by Yb³⁺. In this regime, the absolute increase in ⁴I_{13/2} excited-state population is significant. The role of OH⁻ as a quenching site for ⁴I_{13/2} excitation becomes relevant at Er₂O₃ concentrations >0.2 mol %. Strong internal sample heating is a result of the high absorption rates in Yb³⁺-codoped samples and it is shown not to affect the ⁴I_{13/2} decay.

The study suggests that, from a spectroscopic point of view, aluminosilicate glasses are more favorable than soda-lime-silicates as potential materials for 1.55 μm optical amplifiers both due to their larger inhomogeneous broadening and due to their higher radiative relaxation rate constants. It is also concluded that Yb³⁺ is an efficient sensitizer and can potentially reduce Er³⁺ concentrations in a planar optical waveguide amplifier (POWA) material. The possibility for significant internal sample heating in Yb³⁺-codoped samples has to be addressed in the design of a POWA device in order to avoid degradation of the performance of the waveguide by thermomechanical stress.

ACKNOWLEDGMENTS

We thank William H. Grodkiewicz, formerly of AT&T Bell Laboratories, for assistance with glass sample preparation, and John R. Quagliano, Los Alamos National Laboratory, for assistance with YAG:Er³⁺ oscillator-strength calculations.

*Present address: Optical Sciences, The University of Michigan, 1301 Beal Ave., Ann Arbor, MI 48109-2122.

†Present address: Deacon Research, 2440 Embarcadero Way, Palo Alto, CA 94303-3313.

¹P. Cochrane, R. Heckingbottom, and D. Heatley, *Opt. Photonics News* **8**, 15 (1994).

²E. Desurvire, *Erbium-Doped Fiber Amplifiers* (Wiley, New York, 1994).

³O. Lumpholt, T. Rasmussen, and A. Bjarklev, *Electron. Lett.* **29**, 495 (1993).

⁴M. Federighi, I. Massarek, and P. F. Trwoga, *IEEE Photonics Technol. Lett.* **5**, 227 (1993).

⁵E. Snoeks, G. N. van den Hoven, and A. Polman, *J. Appl. Phys.* **73**, 8179 (1993).

⁶R. S. Quimby, W. J. Miniscalco, and B. Thompson, *J. Appl. Phys.* **76**, 4472 (1994).

⁷H. K. Kim, C. C. Li, X. M. Fang, Y. Li, D. W. Langer, and J. Solomon, *J. Lumin.* **60&61**, 220 (1994).

⁸M. Federighi and F. Di Pasquale, *IEEE Photonics Technol. Lett.* **7**, 303 (1995).

⁹F. Di Pasquale and M. Federighi, *J. Lightwave Technol.* **13**, 1858 (1995).

¹⁰T. Kitagawa, K. Hattori, K. Shuto, M. Yasu, M. Kobayashi, and M. Horiguchi, *Electron. Lett.* **28**, 1818 (1992).

¹¹K. Hattori, T. Kitagawa, M. Oguma, M. Wada, J. Temmyo, and M. Horiguchi, *Electron. Lett.* **29**, 357 (1993).

¹²G. Nykolak, M. Haner, P. C. Becker, J. Shmulovich, and Y. H. Wong, *IEEE Photonics Technol. Lett.* **5**, 1185 (1993).

¹³F. E. Auzel, *Proc. IEEE* **61**, 758 (1973).

¹⁴M. P. Hehlen, *J. Opt. Soc. Am. B* **14**, 1312 (1997).

¹⁵J. A. Caird, A. J. Ramponi, and P. R. Staver, *J. Opt. Soc. Am. B* **7**, 1391 (1991).

¹⁶V. H. Scholtze, *Glastechn. Ber.* **32**, 81 (1959).

¹⁷J. B. Gruber, J. R. Quagliano, M. F. Reid, F. S. Richardson, M. E. Hills, M. D. Seltzer, S. B. Stevens, C. A. Morrison, and T. H. Allik, *Phys. Rev. B* **48**, 15 561 (1993).

¹⁸B. R. Judd, *Phys. Rev.* **127**, 750 (1962).

¹⁹G. S. Ofelt, *J. Chem. Phys.* **37**, 511 (1962).

²⁰B. R. Judd, *Operator Techniques in Atomic Spectroscopy* (McGraw-Hill, New York, 1963).

²¹C. K. Jørgensen and R. Reisfeld, *J. Less-Common Met.* **93**, 107 (1983).

²²D. M. Gruen, C. W. DeKock, and R. L. McBeth, *Adv. Chem. Ser.* **71**, 102 (1967).

²³S. F. Mason, *Struct. Bonding* (Berlin), **39**, 43 (1980).

²⁴J. M. F. van Dijk and M. F. H. Schuurmans, *J. Chem. Phys.* **78**, 5317 (1983).

²⁵T. Miyakawa and D. L. Dexter, *Phys. Rev. B* **1**, 2961 (1970).

²⁶R. Orbach, in *Optical Properties of Ions in Solids*, edited by B. Di Bartolo (Plenum, New York, 1975), p. 355.

²⁷E. I. Kamitsos, J. A. Kapoutsis, H. Jain, and C. H. Hsieh, *J. Non-Cryst. Solids* **171**, 31 (1994).

²⁸N. J. Cockroft, G. D. Jones, and D. C. Nguyen, *Phys. Rev. B* **45**, 5187 (1992).

²⁹M. P. Hehlen, G. Frei, and H. U. Güdel, *Phys. Rev. B* **50**, 16 264 (1994).

³⁰A. J. Bruce, W. A. Reed, A. E. Neeves, L. R. Copeland, W. H. Grodkiewicz, and A. Lidgard, in *Optical Waveguide Materials*, edited by M. M. Broer *et al.*, MRS Symposia Proceedings No. 244 (Materials Research Society, Pittsburgh, 1992), p. 157.

³¹S. A. Brawer and W. B. White, *J. Chem. Phys.* **63**, 2421 (1975).

³²T. Furukawa and W. B. White, *J. Non-Cryst. Solids* **38&39**, 87 (1980).

- ³³T. Furukawa, K. E. Fox, and W. B. White, *J. Chem. Phys.* **75**, 3226 (1981).
- ³⁴M. P. Hehlen, N. J. Cockroft, T. R. Gosnell, A. J. Bruce, G. Nykolak, and J. Shmulovich, *Opt. Lett.* **22**, 772 (1997).
- ³⁵R. K. Watts and H. J. Richter, *Phys. Rev. B* **6**, 1584 (1972).
- ³⁶P. A. Krug, M. G. Sceats, G. R. Atkins, S. C. Guy, and S. B. Poole, *Opt. Lett.* **16**, 1976 (1991).
- ³⁷E. Maurice, G. Monnom, B. Dussardier, A. Saissy, and D. B. Ostrowsky, *Opt. Lett.* **19**, 990 (1994).
- ³⁸M. F. Reid and F. S. Richardson, *J. Chem. Phys.* **79**, 5735 (1983).
- ³⁹*Handbook of Chemistry and Physics* (CRC Press, Boca Raton, 1996).